Enhancing the absolute instability of a boundary layer by adding a far-away plate

J. J. HEALEY

Department of Mathematics, Keele University, Keele, ST5 5BG, UK
j.j.healey@keele.ac.uk

When a solid plate, with a boundary condition of no normal flow through it, is introduced parallel to a shear layer it is normally expected to exert a stabilizing influence on any inviscid linearly unstable waves. In this paper we present an example of an absolutely unstable boundary-layer flow that can be made more absolutely unstable by the addition of a plate parallel to the original flow and far from the boundary layer itself. In particular, the addition of the plate is found to increase the growth rate of the absolute instability of the original boundary-layer flow by an order of magnitude for long waves. This phenomenon is illustrated using piecewise-linear inviscid basic-flow profiles, for which analytical dispersion relations have been derived. Long-wave stability theories have been developed in several limits clarifying the mechanisms underlying the behaviour and establishing its generic nature. The class of flows expected to exhibit this phenomenon includes a class found recently to have an exponential growth of disturbances in the wall-normal direction, owing to the approach of certain saddle-points to certain branch-cuts in the complex-wavenumber plane. The theory also suggests that a convectively unstable flow in an infinite domain can be converted, in some circumstances, into an absolutely unstable flow when the domain is made finite by the addition of a plate, however far away the plate is.

1. Introduction

This paper is concerned with the effect on an absolutely unstable boundary layer of adding a solid plate parallel to the boundary layer and well outside it. The addition of a solid boundary that makes a flow domain finite in the direction normal to the flow is usually expected to exert a stabilizing influence on any inviscid linearly unstable waves. Indeed, in general, the more restricted the domain the more stabilized the flow is expected to be; see for example § 23.3 of Drazin & Reid (1981) or the experiments of Shair *et al.* (1963) on the effects of confinement on the stability of the wake behind a circular cylinder.

We wish to understand some of the differences in stability characteristics between flows that are infinite in the direction normal to a flow, e.g. boundary layers, jets, wakes and free mixing layers, which we shall call unconfined flows, and those that are finite in that direction, e.g. channel and pipe flows, which we shall call confined flows (even though they are all treated as unconfined in the direction of flow). This terminology follows that used by Escudier, Bornstein & Maxworthy (1982) in a study of the effects of confinement in experiments on the vortex-breakdown phenomenon. The focus will be on the qualitative and quantitative changes arising when an unconfined flow is confined. In practice, at least in laboratory experiments, there are no truly unconfined

flows; for example, a boundary-layer flow in a wind tunnel is usually modelled as unconfined in the wall-normal direction but is, of course, confined by the walls of the wind tunnel itself. What seems clear, however, is that if the outer wall is far enough away from the location of the shear layer then the presence or otherwise of the outer wall should have only a small influence on the stability of the flow (if this were not the case, the unconfined-flow model would have been abandoned long ago).

Nonetheless, we present here a flow where the inclusion of an outer wall has a strongly destabilizing effect on the flow, however far from the shear layer that wall is placed. This behaviour arises from an important qualitative change that occurs to the dispersion relation, in which the continuous spectrum of the unconfined flow is replaced by the infinite discrete spectrum of the confined flow created by the addition of the outer wall. This change occurs however far the outer wall is placed from the shear layer. We now briefly explain the origin of this qualitative change in the dispersion relation, because it is central to the behaviour reported in this paper.

The continuous spectrum of interest is produced by branch-cuts introduced to define the roots of square-root functions in the solution to the stability equation in the uniform flow outside the shear layer. To be more specific, we focus for now on the simple case of waves $v(y)\exp[i(\alpha x - \omega t)]$ in an inviscid linearized system, where v is the velocity component of the wave in the (wall-normal) y-direction, t is time, α is the wavenumber, ω is the angular frequency and the basic flow $U(y)$ is in the x-direction. The waves are described in Cartesian coordinates by the Rayleigh equation

$$v'' - \left(\frac{U''}{U-c} + \alpha^2 \right) v = 0, \tag{1.1}$$

where $c = \omega/\alpha$ is the phase velocity of the wave; see Drazin & Reid (1981). When the basic flow is a boundary layer over a plate at $y = 0$, with $\lim_{y\to\infty} U = U_\infty$, then for waves with $c \neq U_\infty$ the Rayleigh equation at large y reduces to

$$v'' - \alpha^2 v = 0, \tag{1.2}$$

with general solution

$$v = C_1 \exp(-\sqrt{\alpha^2} y) + C_2 \exp(\sqrt{\alpha^2} y). \tag{1.3}$$

The square-root symbol is taken to denote the root with positive real part, which corresponds to taking branch-cuts along the imaginary axes of the complex α-plane. There are also branch-cuts generating other continuous spectra associated with the logarithmic behaviour near critical points, where $U = c$, but we are concerned here with the branch-cuts of the square roots in the solution outside the boundary layer.

Our choice for the definition of the square root means that the homogeneous outer boundary condition for the unconfined boundary-layer flow, $\lim_{y\to\infty} v = 0$, is satisfied by choosing $C_2 = 0$, which gives

$$v = C_1 \exp(-\sqrt{\alpha^2} y). \tag{1.4}$$

However, if a plate is placed at a large height $y = h$ above the boundary layer, to produce a confined flow, then the outer boundary condition is replaced by $v(h) = 0$ (in the viscous case, the plate would be taken to be moving at speed U_∞ so as not to introduce a boundary layer at the new plate, but it need not be moving in the present inviscid case because a slip velocity is allowed at the plate). Applying this boundary condition to (1.3) gives a solution of the form

$$v = C_1' \sinh[\sqrt{\alpha^2}(y - h)]. \tag{1.5}$$

Both (1.4) and (1.5) are non-analytic at the branch-cuts used to define the square roots, but it does not necessarily follow that the dispersion relations associated with these solutions will also be non-analytic at the branch-cuts. Consider a solution at a point near a branch-cut in the complex α-plane. If the branch-cut is moved across this point then the roots of the square-root function will be interchanged, i.e. $\sqrt{\alpha^2} \to -\sqrt{\alpha^2}$. Under this transformation (1.4) fails to satisfy the same outer boundary condition for unconfined flow (the boundary condition changes from one of exponential decay, $v' = -\sqrt{\alpha^2}v$, at large y, to one of exponential growth, $v' = \sqrt{\alpha^2}v$), and so its dispersion relation, which depends on the boundary conditions, changes discontinuously. The dispersion relation of the unconfined flow is therefore non-analytic at the branch-cut. However, (1.5) still satisfies the same outer boundary condition, $v(h) = 0$, under this transformation and therefore its dispersion relation is unaffected and so is analytic at the branch-cut of $\sqrt{\alpha^2}$. An explicit example is presented in §3 confirming that the introduction of a plate far from a boundary layer has the effect of removing the branch-cuts due to these square-root functions from the dispersion relation.

Note also that at the imaginary axes of the complex α-plane the 'sinh' in (1.5) becomes 'sin', and the oscillatory form of the solution for the confined flow produces infinitely many roots of the dispersion relation (rather like the standing waves on a finite length of string or in an organ pipe). The presence of this infinity of normal modes is also shown explicitly in the example in §3.

The qualitative difference between the dispersion relation arising from (1.4), which has a branch-cut, and the dispersion relation arising from (1.5), which does not have this branch-cut, indicates that the addition of an outer plate at large h represents a singular perturbation to the dispersion relation. In fact, the presence of the plate makes only an exponentially small perturbation to the roots of the dispersion relation for large h, except in a thin region where $\mathrm{Re}(\alpha) = O(1/h)$, within which the plate makes an $O(1)$ change in the dispersion relation. The reason is that the solution (1.4) decays over a distance $y = O(1/\mathrm{Re}(\alpha))$ and so does not feel the effect of the plate if $h \gg 1/\mathrm{Re}(\alpha)$ but does if $h = O(1/\mathrm{Re}(\alpha))$.

We now consider an unconfined boundary-layer flow, and instability type, which can be expected to be profoundly affected by the introduction of an outer plate, however far away that plate is placed. The flow is disturbed impulsively, but the same considerations would apply to any causal disturbance introduced at some given time. In particular, circumstances have been identified where the faster-growing shorter waves contributing to the impulse propagate away from the source, leaving slower-growing longer waves that are absolutely unstable and grow in the neighbourhood of the source. We will show that these longer waves, and therefore the absolute instability, can be affected by an outer plate placed at any distance from the boundary layer.

The flow exhibiting this behaviour, which will be the subject of this investigation, is the 'rotating-disk boundary-layer' produced when an infinite disk rotates about its axis of symmetry in an otherwise still fluid. Viscous stresses at the disk surface drag the fluid elements near the disk around in almost circular paths, and centrifugal forces cause these elements to spiral outwards. The disk thus acts as a centrifugal fan with a radial flow component that has a wall-jet character directed away from the axis of rotation. The fluid thrown outwards in this way is replaced by an axial flow towards the disk surface. The azimuthal flow component has a typical boundary-layer profile, increasing monotonically from zero at the disk wall to a constant value proportional to the angular velocity of the disk and to the distance to the axis of rotation (when considered, as here, in a frame of reference rotating with the disk). The importance of this crossflow structure to the flow's stability was first recognized by Gregory, Stuart &

Walker (1955), who observed a set of stationary vortices in an experimental study and explained their appearance in terms of an inviscid inflexional 'crossflow' instability. This crossflow instability generates stationary vortices in many three-dimensional boundary layers of engineering interest, and such vortices are believed to be involved in the laminar–turbulent transition process in many of these flows. This provides a strong practical motivation for studying the instability of the rotating-disk boundary layer.

However, our motivation here originates from certain qualitative properties of this instability, discovered more recently, concerning the propagation characteristics of disturbances in the wall-normal direction, see Healey (2006b); these properties make this flow particularly susceptible to the presence, or otherwise, of an outer plate. The present paper builds directly on results of Healey (2006b), and the reader may find it helpful to refer to that work. Long-wave theories for the properties mentioned above, developed in Healey (2005) and Healey (2006a), indicate that they should be present even in a crude model of the rotating disk boundary-layer in which the flow is represented by piecewise-linear segments and in which disturbances are considered in the inviscid limit. We present this model in §2 and show how well it captures the important qualitative features of the instability of the rotating-disk boundary layer. The advantage of the model is that an analytical dispersion relation can be derived, and its roots obtained by a simple Newton iteration, thus avoiding the need for more-slowly-obtained numerical solutions of the Rayleigh equation. The model also facilitates the identification of long-wave scalings for various phenomena, which can in principle be used to obtain long-wave theories for more realistic smooth-velocity profiles.

In §3 the model is adapted by imposing an outer plate at a distance above the boundary layer, and the consequences of the outer plate are investigated. Numerical solutions of an initial-value problem are obtained in §4 confirming the predictions made by the saddle-point theory. Conclusions are drawn in §5.

2. Model for the stability of a rotating-disk boundary layer

In this section we shall outline the derivation of the basic flow solution and Rayleigh equation for a rotating-disk boundary layer. A comprehensive review of the stability of this flow would not be appropriate here, but a few developments that have led to the present investigation into the effect of adding a plate a large distance from the boundary layer will be summarized. For a recent review of the stability and transition of the rotating-disk boundary layer see Saric, Reed & White (2003) and also a forthcoming special issue of *The Journal of Engineering Mathematics* containing experimental, numerical and theoretical studies of instabilities of this flow see Healey (2007).

2.1. *The rotating-disk boundary layer*

Suppose that the disk rotates at constant angular velocity Ω_* in an otherwise still viscous incompressible fluid of kinematic viscosity ν_* (in this paper all dimensional quantities have been given an asterisk subscript). The steady axisymmetric basic flow can be obtained from the von Kármán (1921) similarity solution:

$$u_*(r_*, \theta, z_*, t_*) = r_* \Omega_* U(z), \qquad v_*(r_*, \theta, z_*, t_*) = r_* \Omega_* V(z), \qquad (2.1a,b)$$

$$w_*(r_*, \theta, z_*, t_*) = (\nu_* \Omega_*)^{1/2} W(z), \qquad p_*(r_*, \theta, z_*, t_*) = \rho_* \nu_* \Omega_* P(z), \qquad (2.1c,d)$$

where r_*, θ and z_* are cylindrical coordinates rotating with the disk, which lies at $z_* = 0$; u_*, v_* and w_* are the radial, azimuthal and axial velocity components

respectively; p_* is the pressure, t_* is the time, ρ_* is the constant fluid density and z is the dimensionless axial coordinate scaled on the boundary-layer thickness, $z_* = (\nu_*/\Omega_*)^{1/2}z$.

Substituting equations (2.1) into the Navier–Stokes and continuity equations for incompressible viscous flow in cylindrical coordinates gives a system of nonlinear ordinary differential equations for U, V, W and P. Small-amplitude disturbances are added to this basic flow, the disturbance equations are linearized and, far from the axis of rotation (i.e. many boundary-layer thicknesses from it) a WKB approximation applies and the disturbances take a wavy form proportional to $\exp[iRe(\alpha r + \beta\theta - \omega t)]$ at leading order (we can ignore non-parallel effects in the following inviscid stability analysis). Here $Re = R_*(\Omega_*/\nu_*)^{1/2}$ is the Reynolds number, assumed large, R_* is the distance to the axis of rotation, α is the scaled radial wavenumber, β is the scaled azimuthal wavenumber, ω is the scaled angular frequency and r and t are the scaled radius and time respectively. The appearance of Re in the exponent indicates that the waves are short compared with the distance to the axis of rotation and is the basis of the WKB approximation. In the inviscid limit the disturbance equations reduce to the Rayleigh equation

$$w'' - \left(\frac{Q''}{Q - c} + \gamma^2 \right) w = 0 \tag{2.2}$$

where

$$Q = U + \frac{\beta}{\alpha}V, \quad \gamma^2 = \alpha^2 + \beta^2, \quad c = \frac{\omega}{\alpha}; \tag{2.3a, b, c}$$

$w = w(z)$ is the axial component of the disturbance velocity and the primes denote differentiation with respect to z. Note that βRe is an integer, but since we are working in the large-Re limit we can neglect the implied discretization of β and treat it as a real variable. However, α and ω are both allowed to become complex in the search for eigenvalues that correspond to solutions satisfying the homogeneous boundary conditions

$$w(0) = 0, \quad \lim_{z \to \infty} w(z) = 0. \tag{2.4a, b}$$

See e.g. Healey (2004) for more details (in the notation used in that paper we have taken $\rho = 1$).

Outside the boundary layer, the solution to (2.2) that satisfies the outer boundary condition (2.4b) is proportional to $\exp(-\sqrt{\gamma^2}z)$ when the square-root function, which has branch-points at $\alpha = \pm i\beta$, has its branch cuts lying on the imaginary axes of the complex α-plane and away from the origin, leaving an analytic strip along the real axis of the complex α-plane.

2.2. *Some relevant stability results for the rotating-disk boundary layer*

Most studies of the rotating-disk boundary layer that followed the original work of Gregory *et al.* (1955) have focused on the stationary vortices that dominate flow visualizations. It has been established that these stationary vortices are generated by points of surface roughness and grow in the direction of increasing radius, thus corresponding to a convective instability. However, Lingwood (1995) used the spatio-temporal analysis of Briggs (1964) to show that this flow becomes absolutely unstable far enough from the axis of rotation. In an absolutely unstable flow, impulsive disturbances grow both upstream and downstream of the disturbance source and in time at the location of the source. Briggs' method involved identifying the dominant saddle point (often called the pinch-point) of the dispersion relation in the rest frame;

see Huerre & Monkewitz (1985, 1990) and Huerre (2000) for introductions to, and reviews of, applications of these ideas in fluid mechanics. Lingwood (1995) located the pinch-point using numerical solutions of the Rayleigh equation (2.2) and also of the viscous version of the equation, but in the viscous problem non-parallel terms were ignored.

Healey (2004) included the non-parallel terms in a local absolute-instability theory at asymptotically large Reynolds numbers near the upper branch of the neutral curve for the onset of absolute instability. It was found that there are two saddle points, and that dominance switches between them at a point along the upper branch of the neutral curve. The saddle that is dominant at large Reynolds number on the upper branch of the neutral curve turns out not to be Lingwood's saddle-point, which is dominant around the critical Reynolds number for absolute instability. Therefore, asymptotic descriptions of Lingwood's pinch-point should be sought along the lower branch of the neutral curve for absolute instability, where wavelengths increase as the Reynolds number increases. As a step in this direction, Healey (2006a) derived a long-wave inviscid theory for the pinch-point in the limit $\beta \to 0$. It was found that the pinch-point becomes asymptotically close to the branch-cut along the negative imaginary axis of the complex α-plane and that the integration contour in the complex α-plane used to obtain the impulse response can only reach this saddle, and remain within the valleys of the saddle, if the branch-cut is moved away from the imaginary axis when β is sufficiently small.

Moving the branch-cut from the imaginary axes of the complex α-plane suggests that eigenfunctions that grow exponentially with distance from the boundary layer (sometimes called 'diverging eigenfunctions') can become important in this problem, even though they do not satisfy homogeneous boundary conditions. A detailed numerical study of the Rayleigh equation at numerically small values of β was carried out in Healey (2006b); this allowed solutions to be obtained for larger α and ω than is possible in the long-wave theory. This enabled a global exploration of the complex α-plane that confirmed that the dominant saddle in the long-wave regime is indeed the pinch-point and that the branch-cuts should be moved in order to reach it. A physical interpretation of this behaviour in the spectral plane was also provided. Frames of reference moving in the z-direction away from the disk were considered, and it was shown that saddles with exponentially growing eigenfunctions in fact represent the growth and propagation of disturbances in the wall-normal direction, in much the same way that the more conventional spatial instability theory, with complex wavenumbers, describes propagation and growth in the streamwise direction. Disturbance energy is generated inside the boundary layer and found to propagate out into the free stream in a way that sustains the exponential growth observed outside the boundary layer.

It should be noted, however, that outside the boundary layer, there is no mean flow shear to provide a source of energy for the growth of disturbances and no restoring force to support wave motion. The presence of wave-like disturbances outside the boundary layer is a direct consequence of wave-like disturbances inside the boundary layer, where there is shear to provide energy and a restoring force; the waves outside the boundary layer are extensions of the waves inside the boundary layer. Nonetheless, the notion of the propagation of a disturbance outside the boundary layer is still useful since although the eigenfunctions exist instantaneously in the wall-normal direction, 'information', i.e. the disturbance arising from a particular initial-value problem, still only propagates at finite velocity. In fact, the situation is identical to the more familiar streamwise propagation, in which a disturbance can be expressed as a superposition

of harmonic waves existing instantaneously for all x; nevertheless, the disturbance produced by a localized source still only propagates away from the source at finite velocity in the streamwise direction.

A further possible problem with modes that cross the imaginary-wavenumber axis is that their wavelengths become infinitely long. This might seem to violate the WKB approximation, which is usually justified on the basis that typical wavelengths of disturbances are short compared with length scales over which the basic flow evolves. In fact, this requirement of the relative shortness of wavelengths is sufficient, but not necessary, for the parallel-flow approximation to be applied. In this problem the WKB approximation causes $\partial/\partial r$ to be replaced by $i\alpha + \partial/\partial r$. The flow is approximately parallel when the $\partial/\partial r$ term can be neglected compared with $i\alpha$. If α is real then this requires the wavelengths to be sufficiently short that α is sufficiently large (the usual argument), but in fact it is only necessary for $|\alpha|$ to be sufficiently large, regardless of the size of α_r. Therefore if, as here, α_i is finite then non-parallel effects on the local stability characteristics can be made negligible by increasing the Reynolds number.

Comparisons were also made in Healey (2006b) between in one case numerically evaluated wavepackets using integration paths that do not cross the imaginary axes of the complex α-plane, and in the other case using large-time asymptotic saddle-point theory, in which the contours of the saddle-point (spatial branches), and the saddles themselves, do cross these axes. This confirmed that the physical solution to the initial-value problem does not depend on the location of the branch-cuts as long as they are first placed in accordance with the principle of causality and with radiation conditions in both wall-normal and wall-parallel directions (i.e. branch-cuts on the imaginary-wavenumber axes, integration contours on the real-wavenumber axis and, above all the singularities in the complex-frequency plane) and are not crossed by the integration contour.

However, as will be shown below, when the outer plate is introduced and the branch cut of the square root is replaced by an infinite discrete spectrum (i.e. an infinite number of spatial modes), this discrete spectrum appears along the imaginary axis and, unlike the branch-cut, cannot be moved. This 'freezing' of the location of the branch-cut represents another qualitative difference between confined and unconfined flows. This difference will particularly affect flows, such as the rotating-disk boundary layer for small β, where growth in the wall-normal direction is indicated by unstable saddle points approaching, or crossing, the imaginary axis of the complex-wavenumber plane. Such flows will be strongly affected by addition of an outer plate at any distance from the boundary layer, because the part of the dispersion relation controlling wall-normal growth crosses the imaginary axis and the presence of the outer plate always produces a strong modification of the dispersion relation close to the imaginary axis of the wavenumber plane.

Healey (2005) developed a long-wave theory for the part of the dispersion relation that describes the wall-normal propagation velocities and growth rates. This theory reveals that the part of the spatial branch (the contour in the complex-wavenumber plane of the dispersion relation having a constant imaginary part of the frequency) that crosses the imaginary axis of the wavenumber plane does not depend on the curvature of the basic-velocity profile. However, as the real part of the frequency increases this spatial branch crosses the real axis of the wavenumber plane, and then the curvature of the basic-flow profile becomes important in determining where the spatial branch lies. The long-wave theory of the absolute instability presented in Healey (2006a) showed that the absolute instability is also independent of basic velocity-profile curvature for long enough waves. Therefore, a model velocity profile
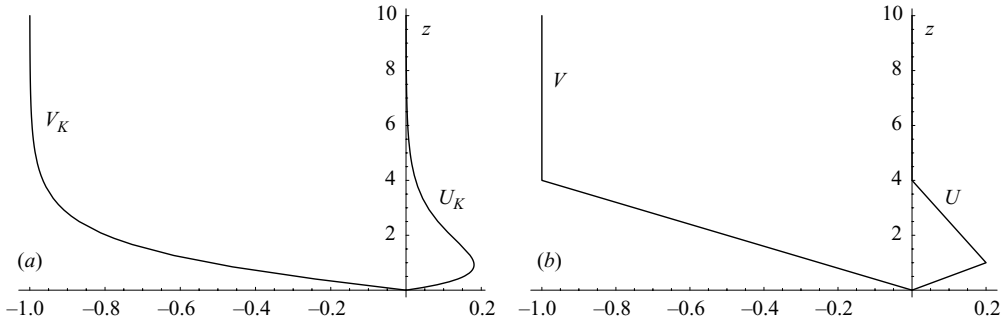
FIGURE 1. (a) Basic flow components (U_K is the radial component, V_K is the azimuthal component) obtained from von Kármán (1921) similarity variables; see Healey (2006a) for the equations and method of solution. (b) The model basic-flow components U and V from (2.5).

with piecewise-linear segments should capture both the absolute instability and the wall-normal growth of the rotating-disk boundary layer but will fail to give the correct qualitative behaviour for shorter waves.

2.3. The model stability problem

On the basis of these considerations, the following model stability problem is proposed to demonstrate how adding an outer plate at a large distance from a shear layer can sometimes dramatically affect the instability characteristics. As discussed above, it models a flow where growth is expected in the wall-normal direction because the dominant saddle point is approaching, or crossing, the imaginary axis of the complex-wavenumber plane. The basic flow has a crossflow structure and axisymmetry, with radial velocity $U(z)$ and azimuthal velocity $V(z)$ modelled by the three-layered system

$$U = \begin{cases} U_1 = \frac{1}{5}z & \text{for} \quad 0 \leqslant z \leqslant 1, \\ U_2 = \frac{1}{15}(4-z) & \text{for} \quad 1 < z \leqslant 4, \\ U_3 = 0 & \text{for} \quad z > 4, \end{cases} \quad V = \begin{cases} V_1 = -\frac{1}{4}z & \text{for} \quad 0 \leqslant z \leqslant 1, \\ V_2 = -\frac{1}{4}z & \text{for} \quad 1 < z \leqslant 4, \\ V_3 = -1 & \text{for} \quad z > 4. \end{cases} \quad (2.5a,b)$$

The form of these expressions has been chosen to make explicit the qualitative wall-jet character of the radial component (the centrifugal-fan effect) and the boundary-layer character of the azimuthual component, of the rotating-disk boundary layer. The actual numerical values of the coefficients were chosen simply to give rough quantitative agreement with the von Kármán similarity solution; see figure 1.

The property $U'' = V'' = 0$ of the piecewise-linear profiles (2.5) means that the Rayleigh equation (2.2) reduces to $w'' - \gamma^2 w = 0$ within each layer, and so the solution satisfying this equation and the boundary conditions (2.4) can be written as

$$w = \begin{cases} w_1 = \sinh(\sqrt{\gamma^2}z) & \text{for} \quad 0 \leqslant z \leqslant 1, \\ w_2 = k_1 \exp(-\sqrt{\gamma^2}z) + k_2 \exp(\sqrt{\gamma^2}z) & \text{for} \quad 1 < z \leqslant 4, \\ w_3 = k_3 \exp(-\sqrt{\gamma^2}z) & \text{for} \quad z > 4, \end{cases} \quad (2.6)$$

where k_1, k_2 and k_3 are constants. These constants are determined by 'jump conditions' that relate the solution in one layer to an adjacent layer, see Drazin & Reid (1981); they correspond to the continuity of pressure across layer boundaries and a condition

that layers neither separate from nor penetrate one another. The jump conditions are

$$\lim_{z \to z_n} \left\{ \left(\frac{w_n}{Q_n - c} - \frac{w_{n+1}}{Q_{n+1} - c} \right) \right\} = 0, \qquad (2.7a)$$

$$\lim_{z \to z_n} \{ [(Q_n - c)w_n' - Q_n' w_n] - [(Q_{n+1} - c)w_{n+1}' - Q_{n+1}' w_{n+1}] \} = 0, \qquad (2.7b)$$

where $Q_n = U_n + (\beta/\alpha)V_n$ and $z = z_n$ is where the layer with subscript n meets the layer with subscript $n + 1$.

Substituting (2.5) and (2.6) into (2.7) for $n = 1$ and $n = 2$ gives four equations for the three unknowns k_1, k_2 and k_3. For these equations to be consistent, a fourth equation, the dispersion relation relating c and α, must also be satisfied. The dispersion relation is a quadratic equation in c (or, equivalently, in ω) but is a transcendental equation in α. We write the dispersion relation as $\Delta(\alpha, \beta, \omega) = 0$; see Appendix A for the definition of Δ.

2.4. *Numerical solutions to the model dispersion relation*

The absolute or convective character of the instability is determined by the dominant saddle point of the dispersion relation. The condition for a saddle point, $\partial\omega/\partial\alpha = 0$, can be expressed as the simultaneous equations $\Delta = \Delta_\alpha = 0$ and solved using Newton iteration for a given β, provided that a good enough first estimate for α and ω is available. An extensive investigation of the complex α-plane is also required in order to identify the dominant saddle, which will be the one with largest $\text{Im}(\omega)$ whose valleys contain the real axes of the complex α-plane for large $|\text{Re}(\alpha)|$ (this is equivalent to identifying the pinch-point in Briggs' method). Figure 2 shows the eigenvalues at the dominant saddle (the pinch-point) when the basic flow is given by (2.5), and also when it is given by the von Kármán similarity solution.

It can be seen that there is excellent qualitative agreement between the pinch-points produced by the two sets of basic velocity profiles, especially as β is reduced. However, the pinch-point remains in the lower-right quadrant of the complex α-plane for the smooth profiles but crosses into the upper-right quadrant for the piecewise-linear profiles for $\beta > 0.065$. This feature might be 'corrected' by a different choice of numerical coefficients in (2.5) or by the addition of one or more layers, but this is not the part of the parameter range that is of interest here. We are concerned with smaller values of β.

The long-wave theory in Healey (2006*a*) shows that, for the pinch-points, $\text{Re}(\alpha) = O(\beta)$ and $\text{Im}(\alpha) = O(\beta^{3/4})$, and so for small β the pinch-point approaches the imaginary α-axis. That theory also shows that the growth rate of the absolute instability is $\text{Im}(\omega) = O(\beta^{9/4})$. However, the long-wave theory in Healey (2005) shows that the strongest growth rate on the negative imaginary axis of the complex α-plane associated with spatial branches originating in the upper half-plane is $\text{Im}(\omega) = O(\beta^2)$, which is larger than that of the absolute instability. It was shown in Healey (2006*b*) that this behaviour in the complex α-plane leads to growth in the wall-normal direction. We anticipate that this wall-normal growth will be strongly affected by the addition of an outer plate and, since all these β-scalings are also true for the piecewise-linear profiles (2.5), they can be used to investigate the effects of adding an outer plate to a flow with wall-normal growth. The results will therefore carry over to the smooth-profile case.

The analysis presented in Healey (2006*b*) shows that moving the branch-cuts away from the imaginary α-axis can be helpful in understanding the behaviour of disturbances in the wall-normal direction, but the exponentially growing 'eigenfunctions'
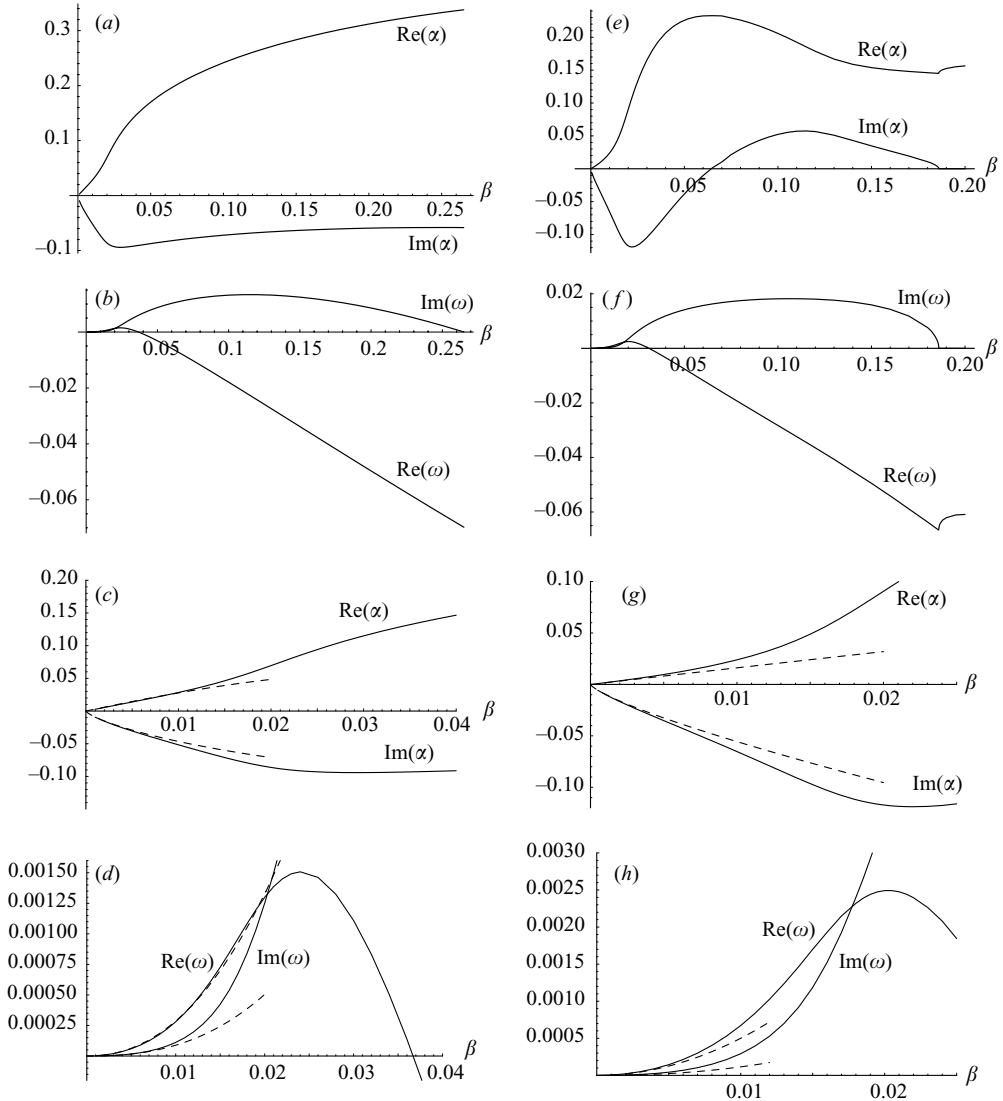
FIGURE 2. The eigenvalues at the pinch-point using the von Kármán solution, (a)–(d), and using the model (2.5), (e)–(h). The solid lines are numerical solutions of dispersion relations, i.e. of (2.2) for the von Kármán profiles and (using Newton iteration) of $(A\,1)$ for the model flow (2.5). The dashed lines correspond to explicit expressions derived in the long-wave limit, (3.26) and (3.27) from Healey $(2006a)$ for (c) and (d) and $(B\,9c)$ and $(B\,9d)$ for (g) and (h). The lower four graphs are enlargements of the regions near the origion in the upper four.

revealed by moving the branch-cuts have no analogue in the corresponding problem in which an outer plate has been added. Therefore, it is of interest to compare the topology of the complex α-plane with, and without, an outer plate. An example of the complex α-plane without an outer plate for modes that decay exponentially with distance from the wall is shown in figure 3. The key feature reproduced by this model flow with piecewise-linear velocity profiles is the proximity of the pinch-point to the imaginary axis of the wavenumber plane. That this behaviour can be captured in such a crude model confirms the robustness of this behaviour, a robustness which was predicted originally by the long-wave theories of Healey (2005) and Healey (2006a).
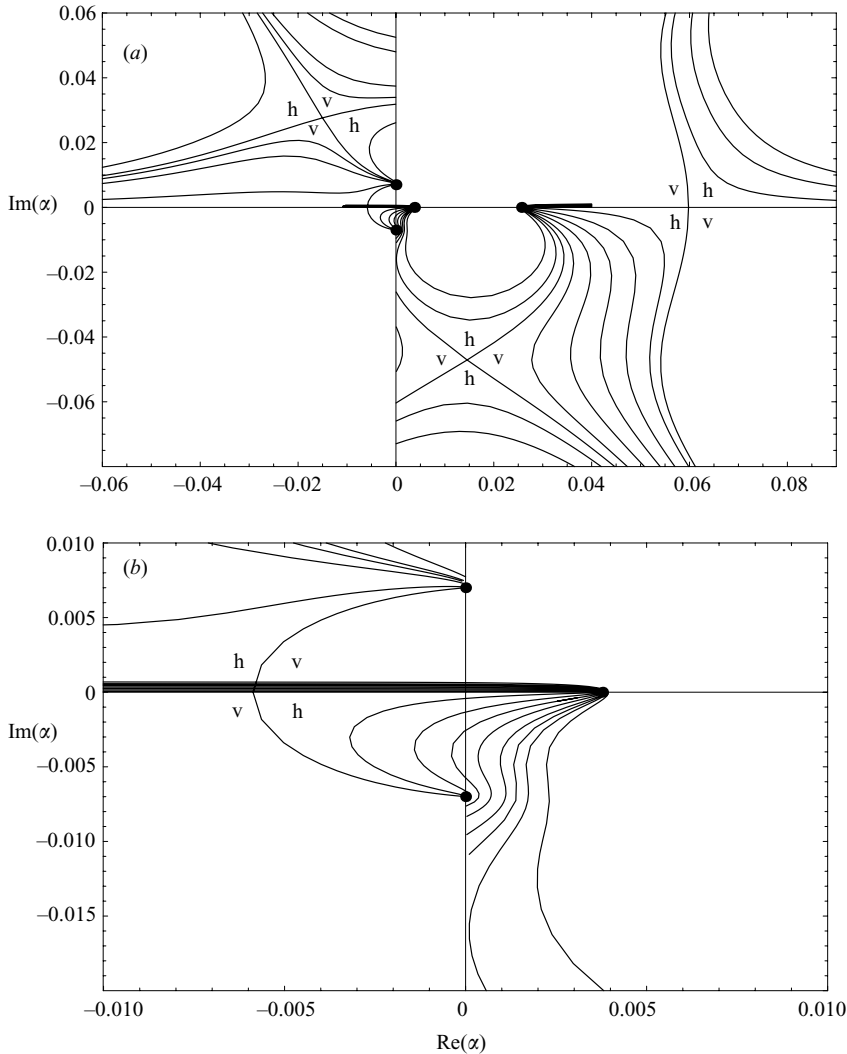
FIGURE 3. Contours of constant $\mathrm{Im}(\omega) \geqslant 0$ for roots of the dispersion relation for unconfined disturbances in the model (2.5), in the complex α-plane for $\beta = 0.007$ and for decaying eigenfunctions. The solid disks show the locations of branch-points. (*b*) is an enlargement of a region near the origin in (*a*). The valleys of saddles are marked with a 'v' and the hills with an 'h'. The branch-cuts from the branch-points at $\alpha = \pm \mathrm{i}\beta$ lie on the imaginary α-axes and radiate away from the origin. No branch-cuts have been drawn from the branch-points on the real α-axes at $\alpha = 0.003\,78$ and $\alpha = 0.025\,67$. The dominant saddle (the pinch-point) lies at $\alpha = 0.0146 - 0.0471\mathrm{i}$ and has $\omega = 0.000\,3000 + 0.000\,1036\,\mathrm{i}$.

The dispersion relation has real coefficients, so the complex conjugates of roots are also roots of the dispersion relation. Surfaces with $\mathrm{Im}(\omega) \leqslant 0$ can therefore be obtained by the reflection of contours in the real α-axis but they are not shown since they would complicate this diagram even further and since our interest in any case lies with the unstable part of the dispersion relation. Contours with $\mathrm{Im}(\omega) = 0$ are invariant under reflection in the real α-axis. The branch-points at $\alpha = \pm \mathrm{i}\beta = \pm 0.007\mathrm{i}$ in figure 3 are where the Riemann surface with exponentially decaying eigenfunctions joins the Riemann surface with 'eigenfunctions' that grow exponentially with distance from the
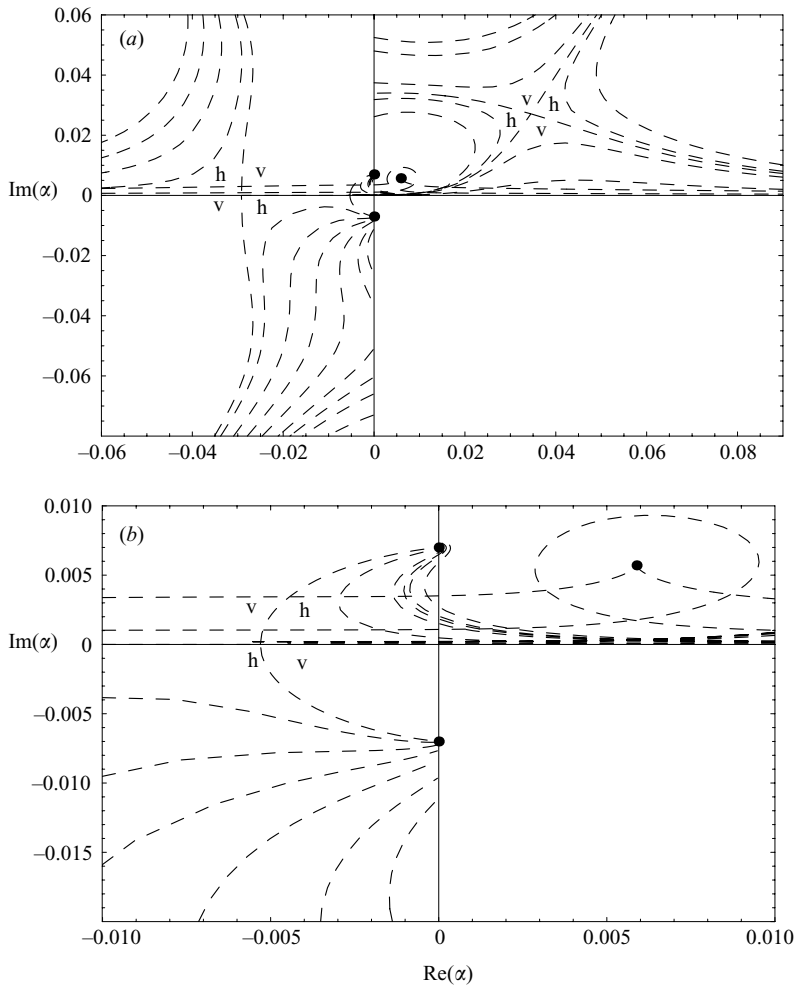
Figure 4. Contours of constant $\text{Im}(\omega) \geqslant 0$, for roots of the dispersion relation for unconfined disturbances in the model (2.5), in the complex α-plane for $\beta = 0.007$ and for eigenfunctions that grow exponentially with distance from the wall (indicated by dashed lines). The solid disks show the locations of branch-points. (*b*) is an enlargement of a region near the origin in (*a*). Valleys of saddles are marked with a 'v' and hills with an 'h'. The branch-cuts from the branch-points at $\alpha = \pm \text{i}\beta$ lie on the imaginary α-axes and radiate away from the origin. The Riemann surface shown in this figure is the analytic continuation of the Rieman surface shown in figure 3 behind these branch-cuts.

plate; branch-cuts have been introduced along the imaginary α-axes to separate these surfaces. The Riemann surfaces with growing eigenfunctions are shown in figure 4 and are the analytic continuations of the surfaces shown in figure 3. There are also branch-points that connect Riemann surfaces of decaying eigenfunctions on the real α-axis at $\alpha \approx 0.003\,78$ (with $\omega \approx -0.000\,617$) and at $\alpha \approx 0.025\,67$ (with $\omega \approx 0.001\,094$), see figure 3. Furthermore, there is a complex conjugate pair of branch-points that connect Riemann surfaces with exponentially growing eigenfunctions; the branch-point with $\text{Im}(\omega) > 0$ lies at $\alpha \approx 0.005\,88 + 0.005\,71\,\text{i}$ (with $\omega \approx -0.000\,159 + 0.000\,660\,\text{i}$) and is shown in figure 4(*b*).

The condition for a branch-point is $\partial\alpha/\partial\omega = 0$, i.e. $\Delta = \Delta_\omega = 0$, and contours from the different Riemann surfaces that join at a branch-point can intersect one another if both surfaces are plotted on the same diagram. Care is required in the interpretation of these diagrams. As discussed above, branch-cuts have been introduced from the branch-points at $\alpha = \pm i\beta$, to define the extent of the Riemann surfaces that meet at these points, in such a way that surfaces of decaying and growing eigenfunctions are shown in separate diagrams (figures 3 and 4). In order to separate out completely all the Riemann surfaces, and thereby to remove all intersections of contours from different surfaces, it would be necessary to introduce further branch-cuts from the remaining branch-points and additional diagrams corresponding to each Riemann surface, as in, for example, figure 3 of Healey (2006*b*). However, in the present case, the branch-points on the real α-axis connect surfaces with $\mathrm{Im}(\omega) \geqslant 0$ to surfaces with $\mathrm{Im}(\omega) \leqslant 0$, and no such intersections appear near these branch-points in figure 3 because only contours with $\mathrm{Im}(\omega) \geqslant 0$ are shown. Nonetheless, it can be noted that the contours become very close to one another in the complex α-plane near these real-axis branch-points, and there are intersections near the real α-axis near the saddle point shown in figure 3(*b*). The branch-point at $\alpha \approx 0.005\,88 + 0.005\,71\,\mathrm{i}$ shown in figure 4 generates more obvious intersections of contours. Note that the contour passing through this branch-point (which has $\mathrm{Im}(\omega) = 0.000\,66$) has a cusp at the branch-point; contours with $\mathrm{Im}(\omega) > 0.000\,66$ would pass above this branch-point in the diagram (though none are shown in figure 4) and contours with $\mathrm{Im}(\omega) < 0.000\,66$ form self-intersecting loops around the branch-point. With these considerations in mind, and given the orientations of the hills and valleys of all the saddles, the topology of the Riemann surfaces can be deduced. Therefore, it is not necessary to present a series of additional diagrams separating out all the Riemann surfaces.

The significance of figure 3 is that it allows the growth rate of disturbances in the rest frame to be determined. Calculating the evolution of an impulsive initial condition into a growing wavepacket requires the evaluation of an integral over all wavenumbers of the unstable normal modes. The path of integration can be taken along the real α-axis on Riemann surfaces of solutions with eigenfunctions that decay in the wall-normal direction. This path can be deformed away from the real α-axis provided that it does not cross branch-cuts or other singularities. At large times this is useful because then the integral is dominated by contributions from neighbourhoods of certain saddle-points. The largest contribution to the solution comes from the highest saddle-point, i.e. the one with largest $\mathrm{Im}(\omega)$, whose valleys can contain the whole path of integration after such an appropriate allowable deformation. (This is the essence of Briggs' method, where this dominant saddle-point is called the 'pinch-point'). The growth rate in the rest frame is given by $\mathrm{Im}(\omega)$ at the dominant saddle-point. If $\mathrm{Im}(\omega) > 0$ for the dominant saddle-point then the flow is called absolutely unstable.

The dominant saddle-point in figure 3 corresponds to the saddle-point predicted by the long-wave theory in Healey (2006*a*) to approach the branch-cut on the imaginary α-axis as $\beta \to 0$. Indeed, the value of β chosen in this diagram is already sufficiently small that, with the chosen arrangement of branch-cuts, this saddle-point can only be reached by taking the integration path down the right-hand side of the branch-cut on the negative imaginary α-axis, and thus outside the valley of the dominant saddle. The branch-cuts contribute a continuous spectrum to the integral and, in this case, the continuous-spectrum contribution is stronger than that of the saddle-point because the branch-cut lies on a part of the Riemann surface that is higher than the saddle-point. Numerical evaluations of the impulse response using such an integration

path were presented in Healey (2006*b*). It was found, surprisingly, that the continuous spectrum produces a growing wavepacket propagating in the wall-normal direction away from the wall and out into the free stream. It was further shown that this behaviour of the continuous spectrum can be understood without having to resort to numerical evaluation of the integral, but instead by simply moving the branch-cut away from the imaginary α-axis and considering waves with growing eigenfunctions. This allows the growth rate, and group velocity, of the wavepacket in the wall-normal direction to be calculated using a saddle-point theory where the saddle-point condition includes terms associated with propagation away from the wall.

Moving the branch-cuts from the imaginary axes under these circumstances and taking integration paths that then cross the imaginary axes thus leads to greater physical understanding of the instability in the unconfined flow. The use of growing eigenfunctions captures the exponential growth of disturbances in the wall-normal direction of initial-value problems for this flow. Figure 5 shows the superposition of the Riemann surfaces obtained by removing the branch-cuts from the imaginary axes and thereby joining the surfaces of growing and decaying eigenfunctions. The integration path then runs from large negative real α on the Riemann surface of decaying eigenfunctions, along the negative real α-axis and then clockwise around the branch-point at $\alpha = -\mathrm{i}\beta$ and onto the Riemann surface of growing eigenfunctions so as to remain within the left-hand valley of the dominant saddle-point. It then moves back onto the Riemann surface of decaying eigenfunctions, over the dominant saddle and onto the positive real-α axis. Equivalently, the integration path could simply follow the contour that passes through the dominant saddle at $\alpha = 0.0146 - 0.0471\,\mathrm{i}$ from above.

However, the next highest saddle-points, at $\alpha \approx -0.0150 + 0.0276\,\mathrm{i}$ and $\alpha \approx 0.0345 + 0.0271\,\mathrm{i}$, do not contribute to the physical solution because the integration path cannot be deformed to pass through them without either leaving the valleys of the saddle-points or crossing the branch-cut nominally placed along the imaginary α-axis in the upper half-plane. The highest saddle-point could be made accessible to the integration path, because moving the branch-cut allows the integration path to cross and then re-cross the imaginary α-axis, thus ultimately returning to the real α-axis on the Riemann surface of solutions with decaying eigenfunctions. But, for the next highest saddle-points, no movement of the branch-cut can achieve this because the integration path would always return to the real α-axis on the Riemann surface of solutions with growing eigenfunctions. Therefore, moving branch-cuts does not necessarily allow a particular saddle-point to be reached by the integration path.

The positions of all the saddle-points and branch-points shown in figure 5 depend on β, as do the heights of the saddle-points. However, the qualitative arrangement shown in this figure persists for arbitrarily long waves, i.e. as $\beta \to 0$, and so is generic over a finite range of β. (The first qualitative change to occur as β is increased above some critical value is that it no longer becomes necessary to move the branch-cut from the negative imaginary α-axis in order for the integration path to reach the dominant saddle, because this saddle then moves away from the imaginary α-axis; see Healey (2006*b*) for a sequence of complex α-planes showing this for smooth profiles and for the physical consequences of this qualitative change). To establish the generality of the results shown in figure 5 for small β, it is not necessary to repeat those calculations for various different numerically small values of β; it is sufficient to present long-wave analytical results for the saddle-points and branch-points. These expressions are given in Appendix B. The analytical results for the dominant saddle point are given along
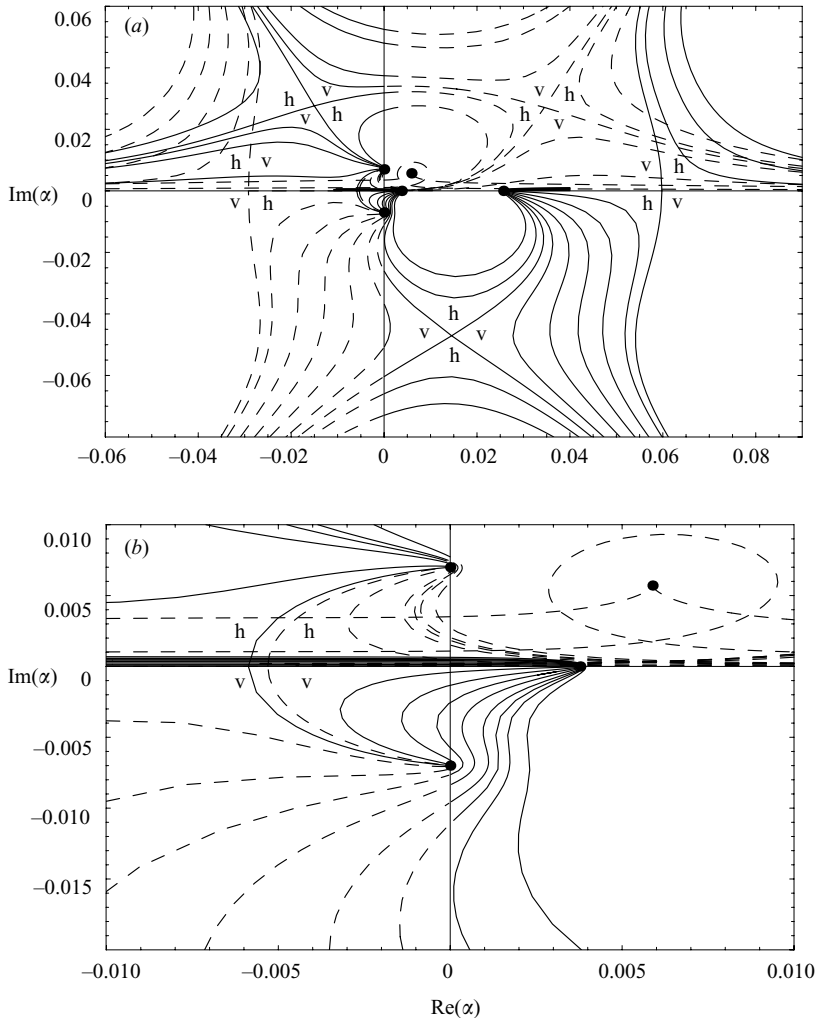
FIGURE 5. Contours of constant $\text{Im}(\omega) \geqslant 0$, for roots of the dispersion relation for unconfined disturbances in the model (2.5), in the complex α-plane for $\beta = 0.007$. The solid lines have eigenfunctions that decay exponentially in the wall-normal direction; the dashed lines have 'eigenfunctions' that grow exponentially in the wall-normal direction. The solid disks show the locations of branch-points. (*b*) is an enlargement of a region near the origin in (*a*). The valleys of saddles are marked with a 'v', and the hills with an 'h'. The pair of saddles close to one another on the negative real α-axis shown in (*b*) are on different Riemann surfaces.

with the numerical roots of the dispersion relation for comparison in figures 2(*g*) and (*h*). The analytical results for the branch points at positive real α shown in figure 3(*a*) and the numerical roots of the dispersion relation are given in figures 6(*a*) and 6(*b*).

In summary, figure 5(*a*) is found to show features that are a distance $O(\beta^{3/4})$ from the origin, while figure 5(*b*) shows features that are $O(\beta)$ from the origin. Remarkably, the simple model basic flow (2.5) generates a total of four branch-points and ten saddle-points in the neighbourhood of the origin as $\beta \to 0$ (those not shown in figure 5 have $\text{Im}(\omega) < 0$). Many of these features are apparent in the numerical Rayleigh solutions for the smooth-velocity profiles presented in Healey (2006*b*); e.g. figure 3 of that paper shows the branch-point (B 3) and the saddle-points
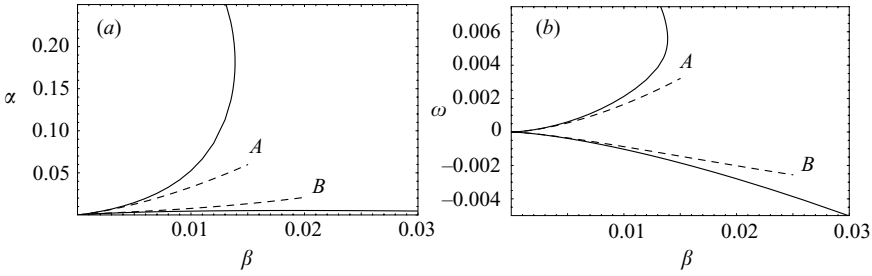
FIGURE 6. Numerical solutions to the dispersion relation for unconfined flow for the pair of branch-points on the real α-axis (solid lines) and, for comparision, the long-wave analytical results (dashed lines). The wavenumbers at the branch points are shown in (a) and the frequencies in (b). Branch-point A is given by (B 3) for small β, and B is given by (B 2) for small β. At $\beta = 0.007$, branch-point A lies at $\alpha = 0.025\,67$ and branch-point B lies at $\alpha = 0.003\,78$ in figure 3.

(B 9) and (B 9) for $\beta = 0.036$, and a distorted version of figure 3 of the present paper can be seen in figure 4(d) of that paper.

As the wavelengths increase, all the branch-points and saddle-points identified here using the piecewise-linear model will correspond more and more closely to branch-points and saddle-points for smooth profiles, because this is the limit in which piecewise-linear profiles give the most accurate stability predictions. This justifies using the model (2.5) to investigate the effect of adding an outer boundary to the disturbances some distance outside the boundary layer, for relatively long waves.

3. Model boundary-layer flow with an outer plate

With an outer plate the basic flow (2.5) is unchanged but the outer boundary condition on disturbances, (2.4b), is replaced by

$$w(h) = 0, \tag{3.1}$$

where $h > 4$. This corresponds to adding a plate at $z = h$ above the boundary layer. Within the inviscid approximation, the axial basic-flow component is neglected in the derivation of (2.2) and so does not appear in the model (2.5) either. The basic flow is therefore not altered at leading order by introducing a plate high above the boundary layer. The solution (2.6) is replaced by

$$
w = \begin{cases}
w_1 = \sinh(\sqrt{\gamma^2}z) & \text{for} \quad 0 \leqslant z \leqslant 1, \\
w_2 = k_1 \exp(-\sqrt{\gamma^2}z) + k_2 \exp(\sqrt{\gamma^2}z) & \text{for} \quad 1 < z \leqslant 4, \\
w_3 = k_3' \sinh[\sqrt{\gamma^2}(z-h)] & \text{for} \quad z > 4,
\end{cases} \tag{3.2}
$$

which satisfies (3.1). Applying the jump conditions (2.7) to the slution (3.2) and eliminating the constants k_1, k_2 and k_3' leads to the dispersion relation for the problem with an outer plate, which we write as $F(\alpha, \beta, \omega, h) = 0$; see Appendix C for the explicit expression.

It can be seen that $F = 0$ is invariant under $\sqrt{\gamma^2} \to -\sqrt{\gamma^2}$, so that essentially the branch-cut associated with this square root has been removed from the dispersion relation, i.e. there are no purely exponentially growing, nor decaying, eigenfunctions. As with Δ, F is quadratic in ω and includes exponentials in α. However, when the outer plate is far enough from the boundary layer, i.e. when

$\mathrm{Re}(\sqrt{\gamma^2})h \gg 1$, $k_3' \sinh[\sqrt{\gamma^2}(z-h)] \sim k_3 \exp(-\sqrt{\gamma^2}z)$ for suitable k_3', except close to $z = h$. Therefore, the dispersion relation $F = 0$ has essentially the same roots as $\Delta = 0$ when $\mathrm{Re}(\sqrt{\gamma^2})h \gg 1$ because then (2.6) and (3.2) differ by only an exponentially small term. This equivalence can also be seen from an examination of the dispersion relations $\Delta = 0$ and $F = 0$ given in Appendices A and C respectively.

Nonetheless, however large h is, sufficiently close to the imaginary α-axis, i.e. when $\mathrm{Re}(\sqrt{\gamma^2}) = O(h^{-1})$ or equivalently when $\mathrm{Re}(\alpha) = O(h^{-1})$, since β is real, the change in outer boundary condition becomes important because then the sinh function cannot be approximated by a single exponential function. The change that this brings about in the dispersion relation close to the imaginary α-axis follows directly from the coefficient of ω^2 in the dispersion relations. The coefficient of ω^2 in Δ has no zeros but in F has the factor $\sinh(\sqrt{\gamma^2}h)$, which has zeros along the imaginary α-axis at

$$\alpha = \pm i \left[\beta^2 + \left(\frac{n\pi}{h} \right)^2 \right]^{1/2}, \tag{3.3}$$

where n is an integer. The significance of (3.3) is that the roots of the dispersion relation $F = 0$ have $|\omega| \to \infty$ at these points in the complex α-plane for all integer n except $n = 0$. These points are therefore the poles of roots of the dispersion relation $\omega = \omega(\alpha)$. In fact, for any given $\mathrm{Im}(\omega)$ there will be an associated contour in the complex α-plane starting, or finishing, on each pole in ω given by (3.3). There are an infinite number of these poles along the imaginary α-axis, and therefore an infinite number of spatial branches (contours of fixed $\mathrm{Im}(\omega)$ in the complex α-plane) near the imaginary α-axis. As $h \to \infty$ the poles become closer to one another and approach $\alpha = \pm i\beta$, where branch-points lie in the unconfined flow, but the interval $-\beta < \mathrm{Im}(\alpha) < \beta$, which is analytic in the unconfined flow, is always free of poles. The accumulation of poles in the singular limit $h \to \infty$ corresponds to the discretization of the branch-cuts that exist in the unconfined problem.

The poles (3.3) are fundamental to the structure of the dispersion relation close to the imaginary axis of the complex α-plane for confined flows. It will be shown below that a pair of branch-points and also a pair of saddle-points can be associated with each pole. The branch-cut in the unconfined flow is therefore replaced in the confined flow by an infinite number of poles, an infinite number of spatial branches, an infinite number of saddle-points and an infinite number of branch-points, which generates an infinite number of additional branch-cuts.

3.1. *Analytical large-h results*

In this subsection we take $h \gg 1$. This allows the structure surrounding each pole to be determined and makes it unnecessary to obtain more than a few sets of numerical solutions to the dispersion relation $F = 0$.

Note that, as mentioned above, the branch-points at $\alpha = \pm i\beta$ in the unconfined flow are not poles in the confined flow even though they correspond to $n = 0$ in (3.3). In the unconfined flow $\omega = 0$ and $\omega = (-1/4 \pm i/5)\beta$ at the branch-points at $\alpha = \pm i\beta$, and, by the addition of an outer plate at large h, these roots are shifted to

$$\omega = -\frac{400}{41} \left(\frac{1}{4} \pm \frac{i}{5} \right) \frac{\beta}{h} + O(h^{-2}), \quad \omega = \left(-\frac{1}{4} \pm \frac{i}{5} \right) \beta + \frac{4(80+59i)}{5 \times 41} \frac{\beta}{h} + O(h^{-2}). \tag{3.4a,b}$$

Therefore the eigenvalues at $\alpha = \pm i\beta$ are subject only to a regular perturbation. The rest of the imaginary axes for $|\mathrm{Im}(\alpha)| > \beta$ are subject to a singular perturbation

by the addition of an outer plate at large h. In what follows, we shall consider neighbourhoods of the imaginary α-axis with $\mathrm{Im}(\alpha) < -\beta$, since figure 5 shows that modifications in this region can affect the integration path through the valleys of the dominant saddle-point.

There are two branch-points associated with the nth pole on the negative imaginary α-axis (their complex conjugates are associated with the nth pole on the positive imaginary α-axis) and the branch-point with $\mathrm{Im}(\omega) > 0$ is found to be given by

$$\alpha = -\mathrm{i}\left[\beta^2 + \left(\frac{n\pi}{h}\right)^2\right]^{1/2}$$

$$-\frac{16}{41^2}(49 - 31\mathrm{i})\left[3(6+\mathrm{i}) - 5(1-\mathrm{i})\sqrt{4+15\mathrm{i}}\right]\frac{(n\pi)^2}{\beta h^3} + O(h^{-4}), \qquad (3.5a)$$

$$\omega = -\frac{1}{104}(5+\mathrm{i})\left(5-\mathrm{i}\sqrt{4+15\mathrm{i}}\right)\beta + O(h^{-1}), \qquad (3.5b)$$

for $n^2 \ll h^3$. At leading order the growth rate at these branch-points, $\mathrm{Im}(\omega) \sim 0.079\,06\,\beta$, is independent of n and h, and $\mathrm{Re}(\alpha) \sim 25.02n^2/(\beta h^3)$, so the branch-points move further from the imaginary α-axis as n increases. Clearly the first term in (3.5a) could be expanded for large h, but we wish to emphasize the relation between the position of these branch-points and the poles given by (3.3).

There are also two saddle-points associated with the nth pole on the negative imaginary α-axis. While the branch-points are a distance $O(h^{-3})$ from each pole, the saddle-points are further away; they are $O(h^{-2})$ from each pole, which is comparable with the distance between poles. The member of each pair with $\mathrm{Im}(\omega) > 0$ is found by substituting

$$\alpha = -\mathrm{i}\left(\beta^2 + \frac{\alpha_s}{h^2}\right)^{1/2} + \cdots, \qquad \omega = \frac{\omega_s}{h} + \cdots \qquad (3.6a,b)$$

into $F = 0$ and $F_\alpha = 0$ (the other saddle-point is found by using $\omega = -(1/4 + \mathrm{i}/5)\beta + \omega_s/h$ instead, but it has $\mathrm{Im}(\omega) < 0$). Eliminating ω_s between $F = 0$ and $F_\alpha = 0$ at leading order in h leads to a transcendental equation for α_s:

$$\sin(2\sqrt{\alpha_s}) = 2\sqrt{\alpha_s}. \qquad (3.7)$$

The frequency at a saddle-point is then given by

$$\omega_s = -\frac{400}{41}\left(\frac{1}{4} - \frac{\mathrm{i}}{5}\right)\sqrt{\alpha_s}\cot(\sqrt{\alpha_s})\beta. \qquad (3.8)$$

There are infinitely many solutions to (3.7), e.g. $\alpha_s \approx 12.14 + 10.38\,\mathrm{i}$, $45.49 + 23.30\mathrm{i}$, $98.95 + 37.61\mathrm{i}$, ... However, an asymptotic solution to (3.7) can be found for large α_s (but not too large; in particular, we require $1 \ll \alpha_s \ll h$); the first few terms are

$$\alpha_s \sim \pi^2 n^2 + \mathrm{i}\pi n \ln(4\pi n) + \frac{\pi^2}{2}n - \frac{1}{4}[\ln(4\pi n)]^2 + \frac{\mathrm{i}\pi - 2}{4}\ln(4\pi n) + \frac{\pi(\pi + 4\mathrm{i})}{16} + \cdots \qquad (3.9)$$

where n is a large integer; it terms out that n need not be very large as (3.9) gives α_s to within a few per cent even for $n = 1$.

The first term in (3.9) corresponds to the nth pole, and the subsequent terms describe with increasing accuracy the position of the saddle-point relative to the nth pole. If the leading-order approximation, $\alpha_s = \pi^2 n^2$, is substituted into (3.8) then a division by zero occurs, as expected, since $\alpha_s = \pi^2 n^2$ corresponds to the nth pole.
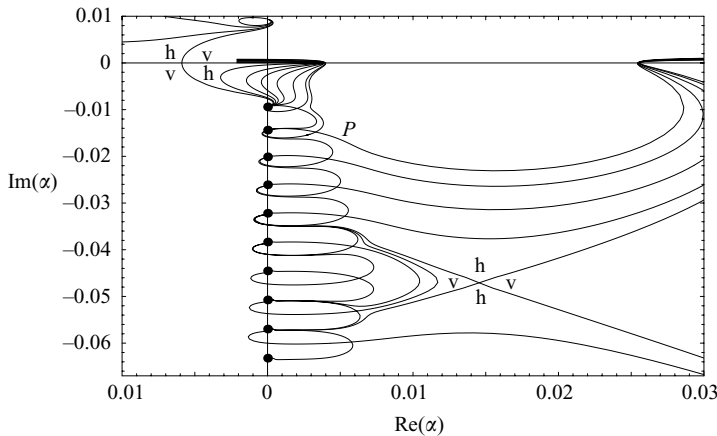
FIGURE 7. Contours of constant $\mathrm{Im}(\omega) \geqslant 0$ for roots of the dispersion relation $F = 0$ in the complex α-plane for $\beta = 0.007$ and with the outer plate at $h = 500$. The solid disks show the locations of poles given by (3.3) for $n = 1, 2, \ldots, 10$ on the imaginary α-axis. As before, the valleys of saddle-points are marked with a 'v' and the hills with an 'h', and the two saddle-points marked in this way correspond to those shown in figure 3. The dominant saddle for this confined problem, labelled P, lies at $\alpha = 0.003\,31 - 0.0148\mathrm{i}$ and has $\omega = 0.000\,1684 + 0.000\,1664\,\mathrm{i}$.

However, substituting the whole of (3.9) into (3.8) leads to

$$\omega_s \sim \frac{400}{41} \left(\frac{1}{5} + \frac{\mathrm{i}}{4} \right) \beta \left[\pi n + \frac{\mathrm{i}}{2} \ln(4\pi n) + \frac{\pi + 2\mathrm{i}}{4} + \cdots \right] \tag{3.10}$$

where we require $n \ll h$ for this result to hold.

These analytical results underpin the following numerical results.

3.2. Numerical results for large finite h

In this subsection we consider the case $\beta = 0.007$, which corresponds to figures 3–5, and take $h = 500$. This value of h is large enough for the position of the saddle that was dominant in figure 3 to be unaffected by the presence of the outer plate but is not so large that the number of poles, branch-points and saddle-points clustered near the imaginary α-axis becomes unmanagable. Figure 7 shows the complex α-plane close to the negative imaginary α-axis. The two saddle-points whose valleys and hills have been indicated lie at $\alpha \approx 0.014\,551 - 0.047\,076\,\mathrm{i}$ and $\alpha \approx -0.005\,8908$. The corresponding values for the unconfined flow are $\alpha \approx 0.014\,552 - 0.047\,074\,\mathrm{i}$ (which is the pinch-point for the unconfined flow) and $\alpha \approx -0.005\,8713$, respectively. The values of ω at these saddle points are also not significantly affected by adding the outer plate, confirming that $h = 500$ is large enough for the outer plate not to affect significantly features away from the imaginary α-axis.

However, as expected, the contours near the imaginary α-axis for $\mathrm{Im}(\alpha) < -\beta$ are dramatically different from those of the unconfined case shown in figure 3. Contours do indeed start and finish on each pole given by (3.3), and a saddle-point with $\mathrm{Im}(\omega) > 0$ can be associated with each pole as predicted by (3.6) and (3.9). These large-h asymptotic predictions for the positions of the saddle-points are accurate enough, at these parameter values, to be used to give first guesses that will allow a Newton iteration to converge on the saddle-points in the numerical solution of $F = F_\alpha = 0$.
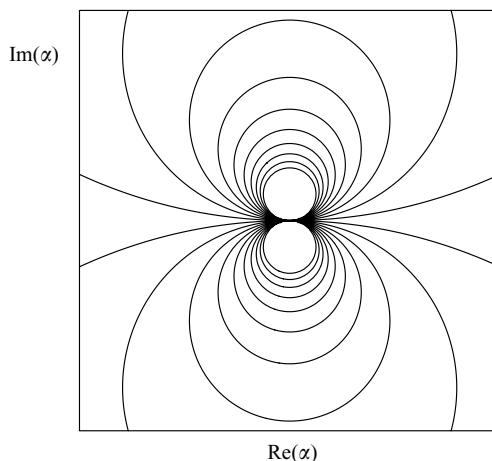
FIGURE 8. Contours of constant Im(ω), i.e. spatial branches, for the model pole $\omega = 1/\alpha$ in the complex α-plane.

The orientation of the hills and valleys of the additional saddle-points can be inferred from the positions of the contours passing through each saddle-point relative to the hills and valleys of the saddle-point at $\alpha \approx 0.014\,551 - 0.047\,076\,\mathrm{i}$. Broadly speaking, the valleys lie above and below the additional saddle-points and their hills lie to the left and right of the saddle-points (however, the lowest additional saddle-point in figure 7 is somewhat rotated). The relative heights of each saddle are also easily deduced: for example, if a contour passing through one saddle lies on the hill of a second saddle then the first saddle lies above the second saddle, etc. Note that there are pairs of contours, emanating from the left of each additional saddle-point, that terminate on the same pole, creating the impression that a maximum has been enclosed by these contours. There can be no maxima or minima of functions of complex variables, but there are families of closed contours close to a pole. Figure 8 shows the dipole structure of the contours of constant Im(ω) for the model pole $\omega = 1/\alpha$. The contours form circles, of various radii, tangent to the origin. In this case contours above the origin with decreasing radius have increasing Im($1/\alpha$), while those below the origin of decreasing radius have increasingly negative Im($1/\alpha$). Sufficiently close to each pole in figure 7 the patterns of contours resemble those in figure 8, the orientation of the axes of symmetry being determined by the argument of the coefficient of the pole.

However, the situation in figure 7 is complicated by the presence of a pair of branch-points close, i.e. of distance $O(h^{-3})$, to each pole. The effect of the branch-points on the contours is to 'pull' the latter close together near the branch-points. Figure 9 shows a selection of contours with Im(ω) > 0 close to the negative imaginary α-axis. The nested closed contours tangent to the middle pole in the diagram are like those in the lower half-plane of figure 8. As Im(ω) decreases, the closed contours expand until they come close to the branch-points and then they 'balloon' out of the gap between the branch-points, expanding rapidly to meet the saddle-point associated with each pole. A further reduction in Im(ω) causes the balloon to burst, and the contours no longer follow closed paths but either connect to adjacent poles or continue away from the imaginary α-axis to join up with the contours that make up the rest of the complex α-plane. If Im(ω) is reduced to negative values then the contours connecting adjacent poles reach a saddle-point in the left half-plane (mentioned just above (3.6)).
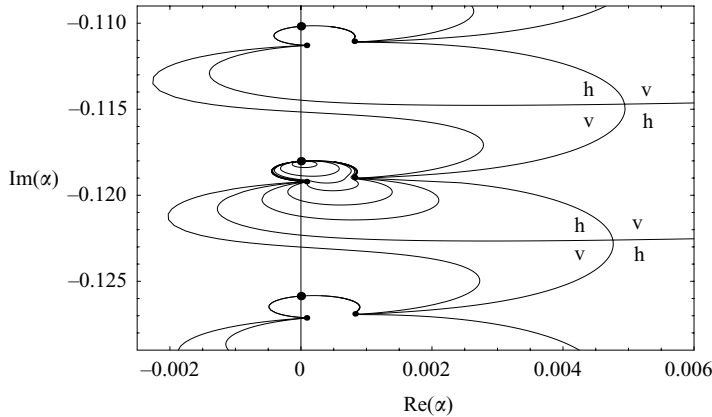
FIGURE 9. Contours of constant $Im(\omega) > 0$ for roots of the dispersion relation $F = 0$ in the complex α-plane for $\beta = 0.007$ and with the outer plate at $h = 400$ (h has been reduced relative to its value in figure 7 to move the branch-points a little further from the imaginary α-axis). The larger solid disks show the locations of the three poles given by (3.3) when $n = 14, 15, 16$ on the imaginary α-axis. The smaller solid disks show the locations of the branch-points predicted by (3.5) and the corresponding branch-points with $Im(\omega) < 0$. The valleys of saddle-points are marked with a 'v' and the hills with an 'h'.

The arrangement of contours around a typical pole with its attendant branch-points and saddle-points, shown in figure 9, constitutes the fundamental building block which, when repeated along the imaginary α-axis infinitely many times, leads to the interlocking structure seen in figure 7 that replaces the single branch-cut of the unconfined problem. This fundamental building block shrinks towards the imaginary α-axis as h increases, in the manner given by the large-h results of § 3.1.

Of fundamental importance is the observation that the pinch-point of figure 3 does not correspond to the pinch-point of figure 7. The pinch-point in figure 7, marked by P, lies at $\alpha \approx 0.003\,307 - 0.014\,80\,i$, and has $\omega \approx 0.000\,1684 + 0.000\,1664\,i$, and so the strength of the absolute instability has been increased by adding an outer plate at $h = 500$ when $\beta = 0.007$ because the pinch-point in the unconfined flow has $Im(\omega) \approx 0.000\,1036$. The pinch-point in this confined flow corresponds to the saddle with $n = 2$ in (3.9). The integration path can follow the highest contour drawn on figure 7 that returns to the real axis.

The mechanism producing the increase in strength of the absolute instability when the outer plate is introduced arises from the property of the dispersion relation for the unconfined flow $\Delta = 0$, which is apparent in figure 3, that the hill above the pinch-point in this figure extends across part of the imaginary α-axis. As explained in Healey (2006b), the contour that is tangent to the imaginary α-axis, yielding a local maximum in temporal growth rate along this α-axis, also gives the growth rate of a wavepacket propagating in the wall-normal direction. When, as here, this growth rate is higher than that of the pinch-point in the unconfined flow, the imposition of an outer boundary will always lead to an increase in the growth rate of the absolute instability because some additional saddles predicted by (3.9) will lie in the hill of the original pinch-point and the highest of these additional saddle-points will become the pinch-point.

It follows that when $h \rightarrow \infty$ and the saddle-points predicted by (3.9) approach the imaginary α-axis, the growth rate of the absolute instability generated by the particular value of n in (3.9) that gives the pinch-point approaches that of the contour
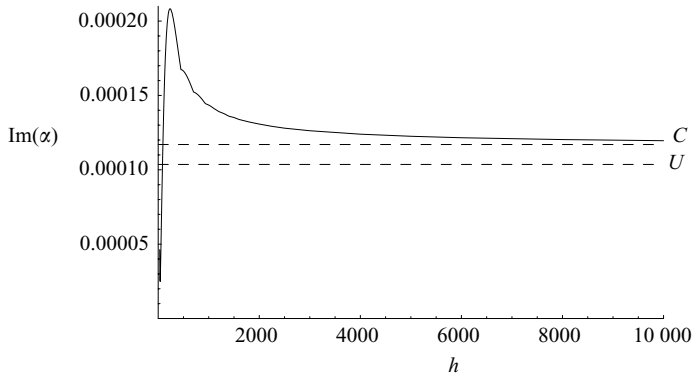
FIGURE 10. The solid line shows how the growth rate of the absolute instability of the confined flow depends on the height h of the plate above the boundary layer for $\beta = 0.007$. The dashed line U gives the growth rate of the absolute instability of the unconfined flow, and the dashed line C gives the growth rate of the convective instability of the unconfined flow propagation in the wall-normal direction; this is seen to be the large-h asymptote of the absolute instability of the confined flow.

that is tangent to the imaginary α-axis in the unconfined flow. In other words, the growth rate of the absolute instability of the confined flow approaches the growth rate of the wavepacket propagating in the wall-normal direction in the unconfined flow as h increases. Therefore, in this case the absolute instability of the confined flow in the limit $h \to \infty$ is different from the absolute instability of the unconfined flow.

These arguments demonstrate that the growth rate of the absolute instability in the confined flow approaches its asymptotic value from above as h increases. However, reducing h eventually has a stabilizing effect on the absolute instability. Figure 10 shows that for $\beta = 0.007$ the maximum growth rate of the absolute instability occurs at $h \approx 235$. At this h the pinch-point corresponds to $n = 1$ in (3.9), but as h increases so does n. The discontinuities in gradient of the curve in figure 10, e.g. at $h \approx 450$, occur when the pinch-point switches from one value of n to an adjacent value of n. This figure also confirms that, for $\beta = 0.007$, as h increases the growth rate of the absolute instability of the confined flow asymptotes towards the growth rate of a wavepacket propagating in the wall-normal direction of the unconfined flow and not towards the growth rate of the absolute instability of the unconfined flow.

The large-h results of §3.1 show how the saddle-points associated with the poles on the imaginary α-axis approach this axis as h increases. Conversely, as h is reduced these saddles move away from the imaginary α-axis and can pass between the saddles of the unconfined flow shown in figure 3. Figure 11 shows the loci, as h is varied, of saddle-points in the part of the complex α-plane near the dominant saddle of the unconfined flow. This figure shows how the pinch-point of the unconfined flow can become surrounded by, and interact with, the additional saddle points created by adding a bounding plate when h is reduced. However, these phenomena associated with more strongly confined flows are beyond the scope of the present work. When h is reduced, eventually the outer plate will have a significant effect on the basic flow and the model (2.5) will become unreliable. This figure for the confined flow also demonstrates an essential connection with figure 3 for the unconfined flow in that as
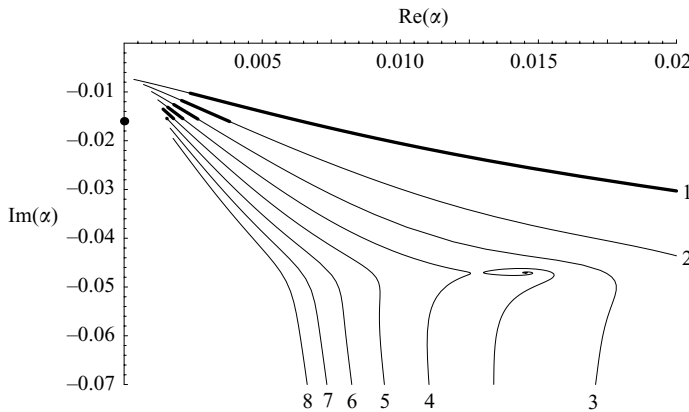
FIGURE 11. The numerical labels of the curves correspond to the values of n in (3.9) for saddle points. As h is reduced, these saddles move down the diagram and away from the imaginary α-axis. The paths of all the saddles are shown for $h \leqslant 1400$ and $\beta = 0.007$. The saddle corresponding to the pinch-point in the unconfined flow spirals around its position in figure 3 as $h \to \infty$. This saddle comes close to the saddle $n = 4$ when $h = 292$. The saddle that is the pinch-point at any given value of h is shown by a bold line. The $n = 1$ saddle is the pinch-point for $h < 448.9$, the $n = 2$ saddle is the pinch-point for $448.9 < h < 698.5$, the $n = 3$ saddle is the pinch-point for $698.5 < h < 934.3$, the $n = 4$ saddle is the pinch-point for $934.3 < h < 1164$, the $n = 5$ saddle is the pinch-point for $1164 < h < 1391$ etc. The disk on the imaginary axis shows where the pinch-point approaches as $h \to \infty$, and corresponds to where the contour in figure 3 (for the unconfined flow) touches the imaginary axis.

$h \to \infty$ the pinch-point of the confined flow approaches the point on the imaginary axis touched by a spatial branch (contour) of the unconfined flow.

3.3. *Long waves and large h*

All the preceding results have been for finite, though numerically small, values of β because this is the range where the dominant saddle of the unconfined flow approaches the imaginary α-axis. The smaller β is, the greater the difference between the growth rate of the absolute instability and the convective growth rate of wall-normal propagating waves of the unconfined flow. Figure 10 shows that this latter growth rate gives the large-h asymptote of the growth rate of the absolute instability of the confined flow, so the lines marked C and U move further apart as β is reduced. In fact, for small β the maximum growth rate shown in figure 10 moves to larger h and can be calculated by linking small β and large h within the following long-wave scalings:

$$\alpha = \alpha_0 \beta + \cdots, \quad \omega = \omega_0 \beta^2 + \cdots, \quad h = \frac{h_0}{\beta} + \cdots \qquad (3.11a,b,c)$$

where $\beta \ll 1$. Substituting (3.11) into $F = F_\alpha = 0$, equating the leading-order terms in β and solving for the dominant saddle that gives the maximum growth rate as h is varied, we obtain

$$\alpha \sim (0.5441 - 1.746\mathrm{i})\beta, \quad \omega \sim (3.190 + 3.506\mathrm{i})\beta^2, \quad h \sim \frac{2.244}{\beta}. \qquad (3.12a,b,c)$$

This growth rate, $\mathrm{Im}(\omega) \sim 3.506\beta^2$, follows the same β-scaling as the growth rate in the limit $h \to \infty$, which is $\mathrm{Im}(\omega) \sim 1.952\beta^2$, obtained using the long-wave theory of Healey (2005) for the growth rate of the wall-normal propagation.

4. Numerical initial-value calculations

As discussed in §2.1, physical disturbances originating from specified initial-value and boundary-value conditions can be expressed as a superposition of normal modes proportional to $\exp[iRe(\alpha r + \beta \theta - \omega t)]$. In particular, the physical solution for the vertical component of the disturbance velocity, $\hat{w}(r, \theta, z, t)$, produced by an impulsive disturbance at $r = r_0$, $t = 0$, $z = 0$, with azimuthal wavenumber $n = \beta Re$, for confined disturbances, is given by an inverse double Fourier transform of the form

$$\hat{w}(r, \theta, z, t) = \frac{e^{in\theta}}{4\pi^2} \int_A \int_B \frac{w(z)}{F} \exp[iRe(\alpha r - \omega t)] \, d\omega \, d\alpha, \qquad (4.1)$$

where $w(z)$ is the solution of the Rayleigh equation for α, β and ω. The integration contours A and B run from $-\infty$ to $+\infty$, A lying along the real axis of the complex α-plane (which is free from singularities because at finite t the disturbance only extends over a finite range of r, ensuring the convergence of the α-integral) and B lying above all singularities in the complex ω-plane, corresponding to the Bromwich contour in Laplace transforms (in oder to respect the principle of causality, i.e. $\hat{w} = 0$ for $t < 0$). This representation of a disturbance in terms of a double integral is discussed in §7.2 of Schmid & Henningson (2001). In principle, a disturbance localized in the azimuthal direction as well can then be constructed by summing over n, but we shall consider only $\beta = 0.007$, the value used earlier in the exploration of the saddle points in the complex α-planes. The dispersion function F must appear in the denominator so that the roots of the dispersion relation $F = 0$ generate poles in the integrand, which give rise to the normal modes of the system by residue theory. Specifically, the ω-integral is evaluated by closing B in the lower half-plane (to give the solution for $t > 0$), and the solution is expressed in terms of the residues of the poles produced by the simple zeros of F to give

$$\hat{w}(r, \theta, z, t) = -\frac{ie^{in\theta}}{2\pi} \int_A \frac{w(z)}{F_\omega} \exp\{iRe[\alpha r - \omega(\alpha)t]\} \, d\alpha, \qquad (4.2)$$

where $\omega = \omega(\alpha)$ is a root of the dispersion relation $F = 0$. In obtaining (4.2), the contribution from the continuous spectrum associated with the logarithmic singularity at critical points (where the phase velocity equals the local mean velocity) has been ignored. In fact, there is no logarithmic singularity for the piecewise-linear model for the mean flow considered here, nor is there a logarithmic singularity for smooth profiles when viscosity is included. If there is more than one unstable temporal mode then the physical solution is a sum of integrals of the type shown in (4.2).

At large times (4.2) is dominated by the contributions made by certain saddle points of the exponent, as identified in figure 3 for unconfined disturbances and in figure 7 for confined disturbances. However, here we evaluate (4.2) numerically to obtain an independent confirmation of the behaviour predicted by the saddle-point analysis, and also to discover the behaviour at finite times. This integral must be evaluated at relatively large t in order to verify the predictions made by the saddle-point theory, and then the integrand is highly oscillatory along part of the positive real α-axis. In order to improve the behaviour of the integrand, so that it can be straightforwardly integrated numerically, the path A is chosen to follow the real α-axis from a large negative value up to $\alpha = 0.0008$; then it drops vertically in the complex α-plane to $\alpha = 0.0008 - 0.047\,07\,i$, and is taken horizontally across the dominant saddle for unconfined disturbances and continued until the integrand has decayed to negligible values. The vertical part of path A, $Re(\alpha) = 0.0008$, runs close
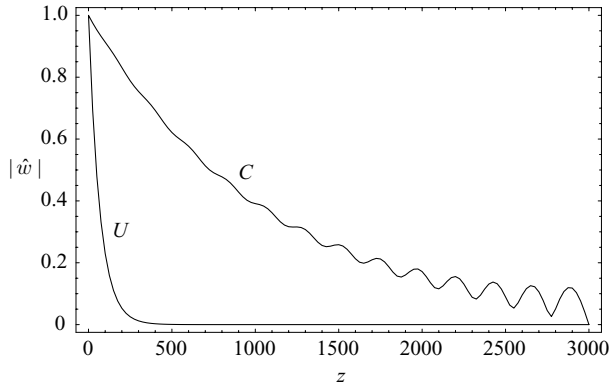
FIGURE 12. U is the eigenfunction for the dominant saddle of the unconfined flow at $\alpha = 0.0146 - 0.0471\mathrm{i}$ in figure 3; C is the eigenfunction for the dominant saddle of the confined flow at $\alpha = 0.003\,31 - 0.0148\mathrm{i}$ in figure 7. Both eigenfunctions have been normalized to give $|\hat{w}(z=4)| = 1$ at the edge of the boundary layer, and they are shown for $4 \leqslant z \leqslant h = 3000$.

to many of the additional saddles created by confinement shown in figure 7, and the horizontal part of the path A, $\mathrm{Im}(\alpha) = -0.047\,07$, picks up the dominant saddle of the unconfined flow.

Roots of the dispersion relation, and F_ω, were evaluated at closely spaced points along A and linear interpolation was used in the intervals between these points to approximate these quantities at arbitrary points on A. The integral (4.2) was evaluated as a sum of integrals over each of these intervals. The number of intervals was varied to ensure convergence over the ranges of t and z used. The outer plate was placed far outside the boundary layer, at $h = 3000$, and the disturbance profile $\hat{w}$ was calculated as a function of z for $r = r_0$ and $\theta = 0$ for times up to $t = 1.35 \times 10^6$.

The disturbance profile is a superposition of eigenfunctions of normal modes but, as time increases, it is expected to become dominated by the normal modes at the dominant saddle points. The eigenfunctions for the dominant saddle points in the confined and unconfined flows are shown in figure 12. The magnitude of the dominant eigenfunction for the unconfined flow decays relatively quickly and monotonically with distance from the boundary layer and has such a small value at $z = h = 3000$ that the addition of the outer plate has only a negligible effect on it. However, the addition of the outer plate generates the additional saddle points shown in figure 7 near the imaginary α-axis, one of which produces the new dominant saddle for the confined flow. Figure 12 shows not only that the eigenfunction of this new saddle decays much more slowly, as expected because it lies closer to the imaginary α-axis, but also that the magnitude of the eigenfuction oscillates as it approaches the outer plate at $z = h = 3000$. This is the result of interference between the two exponential terms that make up the sinh fuction that describes the eigenfunction outside the boundary layer; see (3.2).

A series of graphs showing $|\hat{w}(z)|$ for an impulsive disturbance at a sequence of increasing times is presented in figure 13. It shows how the disturbance profile evolves from a state characteristic of the dominant saddle of the unconfined flow, see 13(a), into a growing wavepacket propagating out of the boundary layer towards the outer plate, see 13(b)–13(f), which is the fundamental property of the unconfined flow that motivated this paper. The qualitative similarity between this initial sequence of diagrams and figure 12 of Healey (2006b) obtained using smooth profiles verifies that
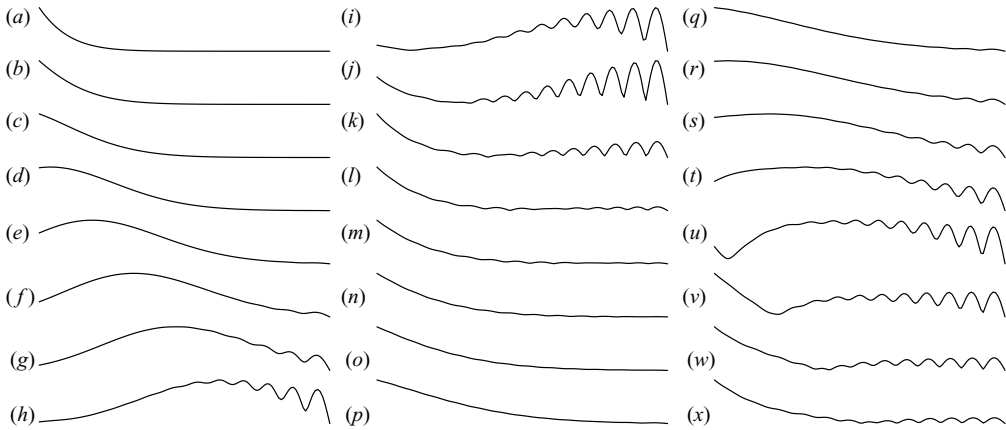
FIGURE 13. Plots of the disturbance magnitude $|\hat{w}|$ as a function of z at successive times. In each plot the vertical axis is rescaled so that the disturbance fills the range (if this is not done, and the same vertical scale used in each plot, then very little of each disturbance would be seen in most of the plots because the amplitude is growing exponentially with time) and the horizontal range is $4 \leqslant z \leqslant h = 3000$. ($a$) is at $t = 2 \times 10^5$, (b) is at $t = 2.5 \times 10^5$, etc. at equal time intervals of 5×10^4 up to (x) at $t = 1.35 \times 10^6$.

the piecewise-linear model makes reliable predictions. As the disturbance approaches the outer plate its magnitude starts to oscillate near the outer plate, see 13(g)–13(k), in a manner similar to that of the dominant saddle of the confined flow. However, there are long-term transients before the disturbance approaches that of the dominant saddle of the unconfined flow. In particular, a second growing wavepacket propagates from the boundary layer out towards the outer plate, see 13(r)–13(v). Even at figure 13(x) the asymptotic large-time behaviour predicted by curve C in figure 12 has probably not yet been reached, although it does show qualitative similarities. However, the transients would die out more quickly for smaller h, as discussed below.

It was shown in Healey (2006b) that the propagation and growth of a wavepacket outside, and away from, an unconfined boundary layer arises from a propagation of energy downstream inside the boundary layer, then out into the free stream and finally back upstream to the streamwise location where the disturbance was introduced; see figure 11 of that paper. Within this context, the appearance of a second outward propagating wavepacket in the confined flow can be interpreted as the result of multiple reflections of parts of the disturbance between the wall adjacent to the boundary layer and the outer plate, though calculations analogous to those in Healey (2006b) have not been carried out to verify this interpretation in detail.

However, the presence of long-term transients can be anticipated from the arrangement of saddle-points near the imaginary α-axis in figure 7. There are many saddles contributing to the physical solution, and they are close to one another in height. Therefore, it takes a long time for the contribution from the highest of these saddles to dominate the contributions from the other saddles. Up until such times the transient behaviour is controlled by interference between the contributions of these saddles, which corresponds to reflections between the plates. It can be noted that, as the separation of the plates is increased, the saddle points near the imaginary axis become closer to one another and closer in height too, so that the period of transient behaviour, i.e. of reflections, increases also.

5. Conclusions

The inviscid stability characteristics of a model boundary-layer flow, based on the rotating-disk boundary layer, have been studied. The effect on the flow's stability of adding a plate, with an impermeable boundary condition, has been investigated. As expected, the continuous spectrum associated with the exponential decay of disturbances in the unconfined flow is replaced by an infinite discrete spectrum when the plate is introduced at a height h above the boundary layer. The main finding is that, for a certain parameter range, the growth rate of the absolute instability of the confined flow as $h \to \infty$ does not tend to the same value as for the unconfined flow. In particular, the growth rate of the absolute instability for the confined flow can be significantly stronger than for the unconfined flow.

The circumstances for this unexpected behaviour to occur have been identified. They are the same circumstances under which disturbances to an unconfined flow will show exponential growth and propagation in the direction across the stream (e.g. in the wall-normal direction for a boundary-layer flow). Healey (2006b) showed that this occurs when the dominant saddle of the dispersion relation (the pinch-point) approaches, or crosses, the imaginary axis of the complex-wavenumber plane. Crossing this imaginary axis, and moving the branch-cut from a square root in the solution accordingly, leads to the consideration of 'eigenfunctions' that grow, instead of decay, exponentially with distance in the wall-normal direction. Healey (2006b) showed that this exponential growth of the eigenfunctions describes the actual exponential growth of initial-value problems. This was shown to happen for inviscid waves of small enough azimuthal wavenumber in the rotating-disk boundary layer, and this observation motivated the present study and the model piecewise-linear flow considered here.

When such a flow is confined by introducing a plate above the boundary layer, the branch-cut of the unconfined flow, which could be moved from the imaginary wavenumber axis to reveal stronger growth rates in the wall-normal direction, is replaced by an infinite discrete spectrum, which cannot be moved from the imaginary axis. Nonetheless, this stronger growth on the Riemann sheet of diverging eigenfunctions still manifests itself when the plate is added. The replacement of the branch-cut by an the infinite discrete spectrum constricts the integration path, forcing it through a region of stronger growth than that of the pinch-point of the unconfined flow. It has been shown that an infinite number of saddle-points is also created when the bounding plate is introduced. One of these saddle-points then has a larger $\mathrm{Im}(\omega)$ than the pinch-point of the unconfined flow and replaces it as the pinch-point of the confined flow. It has been verified numerically that as $h \to \infty$ this new pinch-point of the confined flow has the growth rate of the fastest growing waves of the convective instability in the wall-normal direction of the unconfined flow.

Healey (2006b) showed that the dominant saddle also crosses the imaginary wavenumber in frames of reference moving radially outwards at the leading edge of the wavepacket, but it does not do so in frames of reference moving radially outwards at the velocity of the fastest growing part of the wavepacket. The growth rate of the fastest growing part of the wavepacket corresponds to the growth rate of the most unstable waves in a temporal-stability analysis. This explains why confinement can destabilize an absolute instability (and in this case the instability at the leading edge of the wavepacket too) and yet not affect the most unstable temporal waves, when the plate is far from the boundary layer.

Numerical solutions to the initial-value problem have also been obtained by evaluating inverse Fourier transforms of the solutions in wavenumber and frequency space. These solutions follow qualitatively the predictions of the saddle-point theory

and show that long-term transient behaviour will be present; these consist in part of reflections of the disturbance between the imposed outer plate and the plate adjacent to the boundary layer.

Our findings for an inviscid disturbance, with small scaled azimuthal wavenumbers β, to the model flow (2.5) may be summarized as follows. Applying the theory of Healey (2006a), we find that the growth rate of the absolute instability of the unconfined flow is $\mathrm{Im}(\omega) \sim 4.985\beta^{9/4}$; see (B 9d). Applying the theory of Healey (2005), we find that the unconfined flow supports a convective instability in the wall-normal direction with growth rate $\mathrm{Im}(\omega) \sim 1.952\beta^2$, and this has been shown to be the growth rate of the absolute instability as $h \to \infty$ for fixed small β for the confined flow. The absolute instability for the confined flow is therefore $O(\beta^{-1/4})$ larger than the absolute instability of the unconfined flow as $\beta \to 0$. The strongest absolute instability for the confined flow for small β occurs when $h \sim 2.244/\beta$, giving a growth rate $\mathrm{Im}(\omega) \sim 3.506\beta^2$. These scalings apply to inviscid disturbances to smooth basic-velocity profiles as well (but the numerical coefficients depend on the details of the particular flow under consideration). Note that these asymptotic formulae give respectable quantitative agreement, when evaluated at $\beta = 0.007$, with the numerical results shown in figure 10. The branch-cut of the unconfined flow has been found to be replaced in the confined flow by the interlocking structure of poles, branch-points and saddle-points shown in figure 9, which connects to the rest of the complex-wavenumber plane in the manner shown in figure 7. When the bounding plate is far from the boundary layer, there is a pair of branch-points a distance $O(h^{-3})$ from each pole on the imaginary axis and a pair of saddle-points a distance $O(h^{-2})$ from these each pole, and there are infinitely many such poles.

The physical reason why a plate placed a long way from the boundary layer can have a strong effect on the absolute instability compared with the case of an unconfined flow is that an impulsive disturbance to the boundary layer can produce a disturbance that propagates and grows in the wall-normal direction. If the flow is unconfined then this growing wall-normal part of the disturbance eventually exits the region of interest. However, if the flow is confined by a plate, even one far from the boundary layer, then eventually this growing wall-normal part of the disturbance reaches the plate and sets up a standing wave in the wall-normal direction with an enhanced growth rate of absolute instability, because the greater convective growth in the wall-normal direction of the unconfined flow is converted into the temporal growth rate of the standing wave in the confined flow. Clearly, this mechanism only operates when growth occurs in the wall-normal direction in the unconfined flow, which itself occurs when the dominant saddle approaches, or crosses, the imaginary axis of the complex wavenumber plane.

These results expose a limitation to the familiar concept of a flow that is unconfined in the wall-normal direction. Such flows are confined in practice but, for the cases presented here, the stability characteristics of the corresponding confined flow do not approach the stability characteristics of the unconfined flow as the domain is extended. For these flows, the unconfined-flow problem is a useful model for disturbance propagation for times until disturbances reach the bounding plate, after which, the confined-flow problem must be considered.

The above argument depends on all length scales, including the distance to the plate, h, being small compared with the distance over which the basic flow evolves, and this can be realized, in principle, by increasing the Reynolds number. It is helpful to consider the flow at a fixed physical radius from the axis of rotation, with a plate at a fixed physical height above the disk; then, increasing the Reynolds number (e.g. by

increasing the angular velocity of the disk) will reduce the thickness of the boundary layer and therefore simultaneously improve the parallel-flow approximation (because the wavelengths considered are proportional to the boundary-layer thickness) and also increase h (which is scaled on the boundary-layer thickness). Therefore, by increasing the Reynolds number the limit $h \to \infty$ is approached while maintaining a valid parallel-flow approximation. These inviscid solutions are therefore valid Navier–Stokes solutions at large enough Reynolds numbers. Important issues concerning the relation between these local solutions and global modes, and whether such solutions can be observed at low enough Reynolds numbers for laminar flow to exist in an experiment, will require investigation of the viscous problem, which is beyond the scope of the present work. However, at large Reynolds numbers, non-parallel effects will be larger for the confined flow than for the unconfined flow because the wavenumber of the pinch-point in the confined flow has a smaller magnitude.

Although the present detailed results have been obtained for an inviscid piecewise-linear velocity profile, qualitatively similar behaviour will occur for any flow in which an unstable dominant saddle-point (i.e. pinch-point) crosses, or approaches in the manner described here, the imaginary axis of the complex-wavenumber plane at a point where a branch-cut lies in the unconfined flow. In fact, pinch-points have been found to cross the branch-cuts on the imaginary-wavenumber axis in several other unconfined flows. It may be useful to review these works briefly so that their results may be placed within the context of the present paper.

Huerre & Monkewitz (1985) encountered this behaviour in a smooth mixing-layer flow. When the pinch-point for this flow crosses the imaginary-wavenumber axis, the imaginary part of its frequency is negative, indicating a convectively unstable flow. They simply stated that the left half-plane is of no interest for the evaluation of physical quantities. Lim & Redekopp (1998) encountered this behaviour in a model for swirling jets. They questioned the physical relevance of such a saddle and, while they did not propose an argument for ignoring the saddle, they did not investigate it further. However, they did carry out some calculations for the corresponding confined flow (in which an outer cylinder concentric with the jet is added) and found that confinement could be destabilizing for the absolute instability in some circumstances. Gallaire & Chomaz (2003) suggested that the seemingly non-physical behaviour occuring when the pinch-point crosses the imaginary wavenumber axis in the swirling-jet problem is due to the 'acausal' nature of the model problem, which has discontinuous basic-velocity profiles, resulting in an ill-posed initial-value problem (arbitrarily small-scale disturbances have arbitrarily large growth rates). However, Huerre & Monkewitz (1985), Healey (2006a) and Healey (2006b) all show that a pinch-point can cross, or approach, the imaginary axis of the wavenumber plane in smooth flows, which give causal well-posed initial-value problems.

Yu & Monkewitz (1990) studied the absolute instability of plane jets and wakes with non-uniform density and found a case where the pinch-point approaches the imaginary-wavenumber axis (their figure 7), but they did not comment on the physical significance of this behaviour. Juniper & Candel (2003) studied the effect of confinement on plane wakes with non-uniform density and found that it can destabilize the absolute instability. They also observed saddle-points on, or close to, the imaginary-wavenumber axis (their figure 4), but these were not remarked upon. However, in a more detailed extension of this work, Juniper (2006) found that the pinch-point can cross the imaginary-wavenumber axis. When this happens in the unconfined flow, he ignored this saddle, and when it occurs in the confined flow he called it an 'ambiguous saddle' and again ignored it, even though it satisfies

homogeneous boundary conditions. Several arguments were presented for why these saddles should be ignored. One was based on the presumed breakdown of the parallel-flow assumption (it does not break down if the imaginary part of the wavenumber is finite; see §2.2). Another is based on the failure of these modes to decay with distance outside the shear layer (but we now know that disturbances can grow for a finite distance outside the shear layer see Healey 2006b).

Bearman & Zdravkovich (1978) found that placing a plate near a circular cylinder caused the vortex shedding behind the cylinder to become better defined and more regular. If the shedding pattern is the physical manifestation of a nonlinear global mode resulting from local absolute instability, then it may be that the effect of the confinement is to strengthen the absolute instability and so strengthen the global mode. While the connection (if any) between this problem and the present work is speculative at present, it does raise the question of what the effect of 'semi-confinement', i.e. adding only a single plate to a flow nominally unconfined both above and below the shear layer, will be on the absolute instabilities of plane jets and wakes and mixing layers.

Although saddles have been found that cross the imaginary-wavenumber axis in several different flows, the physical significance of this behaviour was first explained in Healey (2006b). Several studies have noted the unexpected destabilizing effect of confinement for these flows. The present paper, together with Healey (2006b), provides an overarching theoretical framework explaining why confinement will be destabilizing when a pinch-point crosses, or approaches, the imaginary-wavenumber axis in any flow.

Appendix A. Dispersion relation for unconfined flow

Substituting (2.5) and (2.6) into (2.7) for $n = 1$ and $n = 2$ and eliminating k_1, k_2 and k_3 gives the dispersion relation $\Delta = 0$, where

$$\Delta = d_2\omega^2 + d_1\omega + d_0 \tag{A 1}$$

and

$$d_2 = 7200\gamma^2, \tag{A 2}$$

$$d_1 = 60\sqrt{\gamma^2}[3(4\alpha - 5\beta) - 6\sqrt{\gamma^2}(4\alpha - 25\beta) - 16\alpha\exp(-2\sqrt{\gamma^2})$$
$$\qquad + (4\alpha + 15\beta)\exp(-8\sqrt{\gamma^2})], \tag{A 3}$$

$$d_0 = -8\alpha(4\alpha + 15\beta) - 360\beta(4\alpha - 5\beta)\gamma^2 + 3(360\alpha\beta + 91\alpha^2 - 75\gamma^2)\sqrt{\gamma^2}$$
$$\qquad + 8\alpha(4\alpha + 15\beta - 120\beta\sqrt{\gamma^2})\exp(-2\sqrt{\gamma^2}) + 8\alpha(4\alpha + 15\beta)\exp(-6\sqrt{\gamma^2})$$
$$\qquad - (4\alpha + 15\beta)[8\alpha + 3(4\alpha - 5\beta)\sqrt{\gamma^2}]\exp(-8\sqrt{\gamma^2}), \tag{A 4}$$

where $\gamma^2 = \alpha^2 + \beta^2$.

Appendix B. Analytic long-wave solutions for the dispersion relation for unconfined flow

The branch-points in the unconfined flow are found by substituting the expansions

$$\alpha = \alpha_0\beta + \alpha_1\beta^{3/2} + \alpha_2\beta^2 + \cdots, \qquad \omega = \omega_1\beta^{3/2} + \omega_2\beta^2 + \cdots \tag{B 1a, b}$$

into $\Delta = \Delta_\omega = 0$ and then equating coefficients of powers of β and solving the resulting simultaneous equations for α_0, α_1, α_2, ω_1 and ω_2. this leads to asymptotic formulae

for the two branch-points on the real α-axis:

$$\alpha = \frac{5}{4}\beta - 5(41)^{1/4}\beta^{3/2} + \frac{2025}{4\sqrt{41}}\beta^2 + \cdots, \quad \omega = -\frac{(41)^{1/4}}{2}\beta^{3/2} + \frac{25}{\sqrt{41}}\beta^2 + \cdots \quad (B\,2a,b)$$

and

$$\alpha = \frac{5}{4}\beta + 5(41)^{1/4}\beta^{3/2} + \frac{2025}{4\sqrt{41}}\beta^2 + \cdots, \quad \omega = \frac{(41)^{1/4}}{2}\beta^{3/2} + \frac{25}{\sqrt{41}}\beta^2 + \cdots. \quad (B\,3a,b)$$

Note that $\lim_{\beta\to 0} Q_1'(0) = 0$, i.e. the wall shear of the effective basic flow tends to zero for these branch-points in the long-wave limit, see (2.5), where Q_1 is defined below (2.7). The branch-points with exponentially growing eigenfunctions in the wall-normal direction are found by substituting (B 1) into $\Delta = \Delta_\omega = 0$, but with $\sqrt{\gamma^2} \to -\sqrt{\gamma^2}$ in Δ and Δ_ω. Following the same steps as above gives a complex-conjugate pair of branch-points; the one with $\mathrm{Im}(\omega) > 0$ is

$$\alpha = \frac{5}{4}\beta + 5(41)^{1/4}\mathrm{i}\beta^{3/2} - \frac{2025}{4\sqrt{41}}\beta^2 + \cdots, \quad \omega = \frac{(41)^{1/4}\mathrm{i}}{2}\beta^{3/2} - \frac{25}{\sqrt{41}}\beta^2 + \cdots. \quad (B\,4a,b)$$

The two saddle-points shown in figure 5(*b*) can be found by substituting expansions of the form

$$\alpha = \alpha_0\beta + \alpha_1\beta^2 + \cdots, \quad \omega = \omega_0\beta^2 + \omega_1\beta^3 + \cdots \quad (B\,5a,b)$$

into $\Delta = \Delta_\alpha = 0$, and equating coefficients of powers of β than gives

$$\alpha = -\frac{4}{5}\beta - \frac{14\,525\,689}{390\,625\sqrt{41}}\beta^2 + \cdots, \quad \omega = -\frac{20}{\sqrt{41}}\beta^2 + \frac{58\,147\,664}{3\,151\,875}\beta^3 + \cdots \quad (B\,6a,b)$$

for the saddle-point with decaying eigenfunction and, similarly,

$$\alpha = -\frac{4}{5}\beta + \frac{14\,525\,689}{390\,625\sqrt{41}}\beta^2 + \cdots, \quad \omega = \frac{20}{\sqrt{41}}\beta^2 + \frac{58\,147\,664}{3\,151\,875}\beta^3 + \cdots \quad (B\,7a,b)$$

for the saddle-point with growing eigenfunction.

The rest of the saddle-points follow the more exotic scalings discovered by Healey (2006*a*) for smooth velocity profiles:

$$\alpha = \alpha_0\beta^{3/4} + \alpha_1\beta + \cdots, \quad \omega = \omega_0\beta^2 + \omega_1\beta^{9/4} + \cdots. \quad (B\,8a,b)$$

Substituting (B 8) into $\Delta = \Delta_\alpha = 0$, taking $\sqrt{\alpha_0^2} = \alpha_0$ and equating coefficients of powers of β gives four saddle-points; the three with $\mathrm{Im}(\omega) \geqslant 0$ are

$$\alpha = \frac{5^{3/4}}{2}\beta^{3/4} + \frac{199}{120}\beta + \cdots, \quad \omega = 5\beta^2 + \frac{10(5)^{1/4}}{3}\beta^{9/4} + \cdots, \quad (B\,9a,b)$$

$$\alpha = -\frac{5^{3/4}\mathrm{i}}{2}\beta^{3/4} + \frac{199}{120}\beta + \cdots, \quad \omega = 5\beta^2 + \frac{10(5)^{1/4}\mathrm{i}}{3}\beta^{9/4} + \cdots, \quad (B\,9c,d)$$

$$\alpha = -\frac{5^{3/4}}{2}\beta^{3/4} + \frac{199}{120}\beta + \cdots, \quad \omega = 5\beta^2 - \frac{10(5)^{1/4}}{3}\beta^{9/4} + \cdots. \quad (B\,9e,f)$$

Note that the more complicated expansions involving logarithms derived Healey (2006*a*) using matched asymptotic expansions for smooth profiles in reduce to the above results when (2.5) is used for the basic flow, since the present problem has no critical-layer effects.

Substituting (B 8) into $\Delta = \Delta_\alpha = 0$, taking $\sqrt{\alpha_0^2} = -\alpha_0$ and equating coefficients of powers of β gives another four saddle-points; the two with $\mathrm{Im}(\omega) \geqslant 0$ are

$$\alpha = \frac{5^{3/4}}{2}\exp\left(\frac{\pi\mathrm{i}}{4}\right)\beta^{3/4} + \frac{199}{120}\beta + \cdots, \quad \omega = -5\beta^2 + \frac{10(5)^{1/4}}{3}\exp\left(\frac{3\pi\mathrm{i}}{4}\right)\beta^{9/4} + \cdots,$$
$$(\text{B }10a,b)$$

$$\alpha = \frac{5^{3/4}}{2}\exp\left(\frac{3\pi\mathrm{i}}{4}\right)\beta^{3/4} + \frac{199}{120}\beta + \cdots, \quad \omega = -5\beta^2 + \frac{10(5)^{1/4}}{3}\exp\left(\frac{\pi\mathrm{i}}{4}\right)\beta^{9/4} + \cdots.$$
$$(\text{B }10c,d)$$

The five saddle-points given by (B 9) and (B 10) are the five shown in figure 5(a). The scalings (B 8) therefore give rise to a total of eight saddle-points and, as $\beta \to 0$ they approach a circle with radius $O(\beta^{3/4})$ and are equispaced at angles $n\pi/4$, where $n = 0, 1, 2, \ldots, 7$, around the circle; only the five with $\mathrm{Im}(\omega) \geqslant 0$ are shown in figure 5(a).

Appendix C. Dispersion relation for confined flow

Applying the jump conditions (2.7) to equation (3.2) and eliminating the constants k_1, k_2 and k_3' leads to the dispersion relation $F = 0$ for the problem with an outer plate, where

$$F = f_2\omega^2 + f_1\omega + f_0 \tag{C 1}$$

and

$$f_2 = 7200\gamma^2 \sinh(\sqrt{\gamma^2}h), \tag{C 2}$$

$$\begin{aligned} f_1 = 60\sqrt{\gamma^2}\{3(4\alpha - 5\beta)\cosh(\sqrt{\gamma^2}h) - 16\alpha\cosh[\sqrt{\gamma^2}(h-2)] \\ + (4\alpha + 15\beta)\cosh[\sqrt{\gamma^2}(h-8)] - 6(4\alpha - 25\beta)\sqrt{\gamma^2}\sinh(\sqrt{\gamma^2}h)\} \end{aligned} \tag{C 3}$$

$$\begin{aligned} f_0 = -3\sqrt{\gamma^2}\{(4\alpha - 5\beta)(4\alpha + 15\beta)\cosh[\sqrt{\gamma^2}(h-8)] + 320\alpha\beta\cosh[\sqrt{\gamma^2}(h-2)] \\ - (360\alpha\beta + 91\alpha^2 - 75\gamma^2)\cosh(\sqrt{\gamma^2}h)\} - 8\{\alpha(4\alpha + 15\beta)[\sinh(\sqrt{\gamma^2}\{h-8\}) \\ - \sinh(\sqrt{\gamma^2}\{h-6\}) - \sinh(\sqrt{\gamma^2}\{h-2\}) + \sinh(\sqrt{\gamma^2}h)] \\ + 45\beta\gamma^2(4\alpha - 5\beta)\sinh(\sqrt{\gamma^2}h)\} \end{aligned} \tag{C 4}$$

and $\gamma^2 = \alpha^2 + \beta^2$. It can be verified that this dispersion relation becomes asymptotically close to that of the unconfined flow shown in Appendix A when $\mathrm{Re}(\sqrt{\gamma^2}h) \gg 1$.

REFERENCES

BEARMAN, P. W. & ZDRAVKOVICH, M. M. 1978 Flow around a circular cylinder near a plane boundary. *J. Fluid Mech.* **89**, 33–47.

BRIGGS, R. J. 1964 *Electron-Stream Interaction with Plasmas*. MIT Press.

DRAZIN, P. G. & REID, W. H. 1981 *Hydrodynamic Stability Theory*. Cambridge University Press.

ESCUDIER, M. P., BORNSTEIN, J. & MAXWORTHY, T. 1982 The dynamics of confined vortices. *Proc. R. Soc. Lond.* A **382**, 335–360.

GALLAIRE, F. & CHOMAZ, J.-M. 2003 Instability mechanisms in swirling flows. *Phys. Fluids* **15**, 2622–2639.

GREGORY, N., STUART, J. T. & WALKER, W. S. 1955 On the stability of three-dimensional boundary layers with application to the flow due to a rotating disk. *Phil. Trans. R. Soc. Lond.* A **248**, 155–199.

HEALEY, J. J. 2004 On the relation between the viscous and inviscid absolute instabilities of the rotating-disk boundary layer. *J. Fluid Mech.* **511**, 179–199.

HEALEY, J. J. 2005 Long-wave theory for a new convective instability with exponential growth normal to the wall. *Phil. Trans. R. Soc. Lond.* A **363**, 1119–1130.

HEALEY, J. J. 2006*a* Inviscid long-wave theory for the absolute instability of the rotating-disk boundary layer. *Proc. R. Soc. Lond.* A **462**, 1467–1492.

HEALEY, J. J. 2006*b* A new type of convective instability with exponential growth perpendicular to the basic flow. *J. Fluid Mech.* **560**, 279–310.

HEALEY, J. J. 2007 Instabilities of flows due to rotating disks: preface. *J. Engng Maths* **57**, 199–204.

HUERRE, P. 2000 Open shear flow instabilities. In *Developments in Fluid Mechanics: A Collection for the Millenium* (ed. G. K. Batchelor, H. K. Moffatt & M. G. Worster). Cambridge University Press.

HUERRE, P. & MONKEWITZ, P. A. 1985 Absolute and convective instabilities in free shear layers. *J. Fluid Mech.* **159**, 151–168.

HUERRE, P. & MONKEWITZ, P. A. 1990 Local and global instabilities in spatially developing flows. *Annu. Rev. Fluid Mech.* **22**, 473–537.

JUNIPER, M. P. 2006 The effect of confinement on the stability of two-dimensional shear flows. *J. Fluid Mech.* **565**, 171–195.

JUNIPER, M. P. & CANDEL, S. M. 2003 The stability of ducted compound flows and consequences for the geometry of coaxial injectors. *J. Fluid Mech.* **482**, 257–269.

VON KÁRMÁN, TH. 1921 Über laminare und turbulente Reibung. *Z. Angew. Math. Mech.* **1**, 233–252.

LIM, D. W. & REDEKOPP, L. G. 1998 Absolute instability conditions for variable density, swirling jet flows. *Eur. J. Mech.* B *Fluids* **17**, 165–185.

LINGWOOD, R. J. 1995 Absolute instability of the boundary layer on a rotating disk. *J. Fluid Mech.* **299**, 17–33.

SARIC, W. S., REED, H. L. & WHITE, E. B. 2003 Stability and transition of three dimensional boundary layers. *Annu. Rev. Fluid Mech.* **35**, 413–440.

SCHMID, P. J. & HENNINGSON, D. S. 2001 *Stability and Transition in Shear Flows.* Springer.

SHAIR, F. H., GROVE, A. S., PETERSEN, E. E. & ACRIVOS, A. 1963 The effect of confining walls on the stability of the steady wake behind a circular cylinder. *J. Fluid Mech.* **17**, 546–550.

YU, M.-H. & MONKEWITZ, P. A. 1990 The effect of nonuniform density on the absolute instability of two-dimensional inertial jets and wakes. *Phys. Fluids* A **2**, 1175–1181.